energies

MDPI

Article

Numerical Assessments of Flow and Advective Transport Uncertainty for Performance Measures of Radioactive Waste Geological Disposal in Fractured Rocks

Yun-Chen Yu [1,2], Yu-Hsiang Shen [1], Tsai-Ping Lee [3,*], Chuen-Fa Ni [2,4,*] and I-Hsien Lee [4]

1 Institute of Nuclear Energy Research, Atomic Energy Council, Executive Yuan, Taoyuan 32546, Taiwan; yuyc@iner.gov.tw (Y.-C.Y.); andyshens@iner.gov.tw (Y.-H.S.)
2 Graduate Institute of Applied Geology, National Central University, Taoyuan 32001, Taiwan
3 Taiwan Power Company, Taipei 10016, Taiwan
4 Center for Environmental Studies, National Central University, Taoyuan 32001, Taiwan; sfdff327@gmail.com
* Correspondence: u615486@taipower.com.tw (T.-P.L.); nichuenfa@geo.ncu.edu.tw (C.-F.N.); Tel.: +886-2-2365-7210 (ext. 2346) (T.-P.L.); +886-3-422-7151 (ext. 65874) (C.-F.N.)

Abstract: Groundwater flow and transport are crucial for performance and safety assessment in the radioactive waste geological disposal. This study presents the groundwater flow and advective transport simulations for assessing the performance of a reference repository placed in fractured rocks. The study involves the concept of radionuclides migrating into the mobile water in fractures surrounding the deposition hole and calculates two specific quantitative indicators in the field of radioactive waste geological disposal. The indicators equivalent flow rate (Q_{eq}) and flow-related transport resistance (F) are used to express the groundwater flow and transport resistance in the host rock. Based on the hydrogeological conceptual model, the study employs DarcyTools to model the groundwater flow and advective transport of a base case. This study then conducts sensitivity analyses by varying the hydraulic conductivity of the key hydrogeological unit and the excavation damage zone. The uncertainty analysis employs multiple discrete fracture network (DFN) realizations to quantify the influences of DFNs on the flow and advective transport. Results show that the hydraulic conductivity of host rock dominates the flow and advective transport in the model domain, and the highest Q_{eq} is 1.91×10^{-4} m^3/year, and the lowest F is 7.77×10^5 year/m. Results also indicate that simulations of the hydraulic conductivity variations of hydrogeological units are more critical than those obtained from the variations of DFN realizations (i.e., the uncertainty analysis). The solutions could be useful for site investigations to modify the hydrogeological conceptual model in the study.

Keywords: fractured rock; DarcyTools; groundwater flow; advective transport; sensitivity and uncertainty study performance measures

Citation: Yu, Y.-C.; Shen, Y.-H.; Lee, T.-P.; Ni, C.-F.; Lee, I.-H. Numerical Assessments of Flow and Advective Transport Uncertainty for Performance Measures of Radioactive Waste Geological Disposal in Fractured Rocks. *Energies* **2022**, *15*, 5585. https://doi.org/10.3390/en15155585

Academic Editor: Stefan Finsterle

Received: 30 June 2022
Accepted: 28 July 2022
Published: 1 August 2022

1. Introduction

Groundwater flow and characteristics depend highly on the hydraulic conceptual model, e.g., model domain, hydrogeological unit distribution, flow properties of hydrogeological units, and boundary conditions. In addition, the distribution and characteristics of fracture systems are the dominant factors influencing the flow and transport results in fractured rocks. The transmissivity of fractures is recognized to be more significant than that of rock matrix by several orders of magnitude. The large discrepancy of flow properties between fractures and rock matrix has made flow and transport simulation challenging, especially for three-dimensional (3D) large-scale and complex problems [1,2]. The discrete fracture network (DFN) [1–5] and equivalent continuum porous medium (ECPM) [6–8] are two representative models for discrete and continuous approaches, respectively. The DFN model generates the fracture system based on the DFN recipe (i.e., the list composed of the statistic distribution of geometric and flow properties of fractures) to simulate the complex fracture system in fractured rock. The DFN model neglects the contribution of flow and transport by rock matrix and only focuses on the dynamic within fractures in detail, so it is usually employed for problems with complex fracture systems and small-scale domains. However, for a practical problem with a large modeling domain, the DFN model might be computationally expensive because of the generation of the computational mesh and the associated flow and transport simulations.

The ECPM model efficiently addresses problems with large-scale domains, high fracture intensity, and complex hydrogeological units. The ECPM model treats the flow properties in each computational cell as equivalent values by lumping the flow properties of fractures and rock matrices together. The equivalent value in each cell can be considered as a tensor, revealing the anisotropic characteristic of the fractured rock. The ECPM model allows the hydrogeological units and objects embedded in the model domain and assigns the corresponding flow properties. Therefore, the model has been widely used in solving problems with complex conceptual models and large-scale domain in the hydrogeological analysis of geological disposal of radioactive waste in fractured rock. For example, to realize the flow and transport in the candidate site of final radioactive waste disposal in Sweden, the Svensk Kärnbränslehantering AB (SKB) employed the ECPM model to simulate the head distribution and release paths of radionuclides from canister to biosphere in a relatively large-scale domain [9–11].

According to the "Nuclear Materials and Radioactive Waste Management Act" in Taiwan, the radioactive waste producer, Taiwan Power Company (TPC), is responsible for the management, storage, and final disposal of radioactive material, including nuclear source material, nuclear fuel, and radioactive waste [12]. In addition, radioactive waste is classified as spent nuclear fuel (SNF) (SNF is the same as high level waste according to the "Nuclear Materials and Radioactive Waste Management Act" in Taiwan) and low-level waste (LLW) [13]. To fulfill the demands of the regulatory body, TPC has proposed a spent nuclear fuel disposal (SNFD) program since 2005 [14]. TPC adopted the Swedish KBS-3 disposal concept developed by SKB to develop geological disposal technology and capability. The concept involves encapsulating the SNF in copper canisters which are then emplaced, surrounded by the buffer material, which is bentonite clay, in deposition holes at a depth between 400 and 700 m in the bedrock [15]. TPC selected the crystalline rock for research and development purposes and generated a reference case composed of the geological unit and thermal, hydraulic, mechanical, and chemical (THMC) properties and a conceptual disposal facility based on the reference design of the KBS-3 concept. The geological unit and THMC properties refer to the data of field investigation and laboratory experiments of an offshore island in the western part of Taiwan [16]. The data of the reference case is open to the public and researchers who can access the same fundamental information to iterate the technical ability for the radioactive waste disposal project based on experience from the Japanese H12 report [17] and site descriptive model (SDM) concept from SKB [18].

The KBS-3 disposal concept considers groundwater flow and transport characteristics critical factors [9–11,19,20]. The spent nuclear fuel is encapsulated in a corrosion-resistant and load-withstanding copper canister surrounded by buffer in the deposition hole (DH). The KBS-3 disposal concept illustrates three of the safety functions of a canister for containment, including (1) providing corrosion barrier, (2) withstanding isostatic load, and (3) withstanding shear load [20]. The groundwater flow characteristics in the nearby area of and inside the DH, called near-field, play an essential role in calculating buffer erosion and canister corrosion. Once a canister is destroyed, i.e., loses its safety function, the radionuclides will dissolve into the groundwater and migrate from the disposal facility to the humans and the environment, i.e., the biosphere. Therefore, the transport simulation and its trace information in the host rock, i.e., far-field, are necessary for the safety assessment and risk calculation [21].

At this current stage, TPC has adopted the KBS-3 disposal concept to develop the geological disposal technology and capability in Taiwan based on a reference case, and the hydrogeological analysis of flow and transport is one of the critical works for the following performance and safety assessment in the near-field and far-field [16]. This study aims to employ the ECPM model and the computer code, DarcyTools [22–24], for flow and advective transport of a reference case in Taiwan. Specifically, a conceptual disposal facility has been embedded inside the model domain, and the concept of radionuclides released from canisters will also be considered based on the KBS-3 concept [20,21]. An example DFN was firstly generated, and the associated equivalent flow properties in each computational cell calculated. Next, the study simulates the flow field, advective transport, and performance measures (PMs) of the base case with recommended flow properties for hydrogeological units. The PMs are the key parameters for performance and safety assessment in the near-field and far-field based on groundwater flow and advective transport simulation [9–11,19–21]. The study then used a series of cases based on adjusting the lower- and higher-bound of flow properties for each hydrogeological unit. The quantitative comparison of the PMs in each case is conducted based on the safety function indicator of acceptable hydrogeological conditions in the geosphere. Those results are the key factors in evaluating the flow properties of a conceptual disposal facility in the reference case. They are the input data for performance assessment and provide the feedback for the following geological investigation in the radioactive final disposal project [16,21].

2. Materials and Methods

This study employed DarcyTools for modeling the flow and advective transport. The calculations of PMs in the reference case are composed of a hydrogeological conceptual model and a conceptual disposal facility. DarcyTools is a research-based computer code developed by SKB for modeling the flow and transport of a radioactive disposal facility in fractured rocks [22–24]. DarcyTools has been widely used in the radioactive final disposal project in Sweden and Finland. The detailed theory can be obtained through reports and the associated investigations [22–24]. Here, we focus on presenting the fundamental algorithms, such as those governing equations for flow and transport, particle tracking method, and DFN generation in the DarcyTools. In addition, we present the reference case for flow and advective transport simulations and calculations of PMs in this study.

2.1. Mathematical Formulations

2.1.1. Conservation and State Laws

DarcyTools uses the mass conservation equation expressed as below for the case of water and solids [22–27]:

$$\frac{\partial \rho \phi}{\partial t} + \frac{\partial}{\partial x}(\rho u) + \frac{\partial}{\partial y}(\rho v) + \frac{\partial}{\partial z}(\rho w) = Q \tag{1}$$

where ρ is the density (kg/m^3), ϕ is the porosity (-), t is the time (s), and u, v, and w are the directional components of the Darcy velocity (m/s). Notations x, y, and z are the location in a Cartesian coordinate system (m), and Q is the source/sink term per volume of fluid mass [$kg/(m^3s)$]. In DarcyTools, the mass conservation equation of the chemical species is expressed as:

$$\begin{aligned}\frac{\partial \rho \phi C}{\partial t} + \frac{\partial}{\partial x}\left(\rho u C - \rho \gamma D_x \frac{\partial C}{\partial x}\right) + \frac{\partial}{\partial y}\left(\rho v C - \rho \gamma D_y \frac{\partial C}{\partial y}\right) + \frac{\partial}{\partial z}\left(\rho w C - \rho \gamma D_z \frac{\partial C}{\partial z}\right) \\ = QC + Q_c\end{aligned} \tag{2}$$

where C is the transport mass fraction (-), γ is the compaction coefficient (-), and D_x, D_y, and D_z are the normal terms of diffusion-dispersion tensor (m^2/s). Notation Q_c is the source/sink term representing the exchange with immobile zones [($kg/(m^3s)$]. DarcyTools assesses the physical meaning of a change in volume due to a change in pressure by the following expression:

$$\phi = \phi_0 \gamma \tag{3}$$

$$\gamma = 1 + \frac{S_s}{\phi_0} \frac{(P - P_0)}{\rho g} \tag{4}$$

where ϕ_0 is the reference porosity (-) given for a referenced dynamic pressure P_0 [kg/(ms^2)]. The S_s is the specific storage (1/m), P is the dynamic pressure [kg/(ms^2)], and g is the gravity acceleration (m/s^2). The Darcy velocity of the mass conservation equation and the mass transport equation can be rewritten based on Darcy's law as follows:

$$\rho u = -\frac{K_x}{g} \frac{\partial P}{\partial x} \tag{5}$$

$$\rho v = -\frac{K_y}{g} \frac{\partial P}{\partial y} \tag{6}$$

$$\rho w = -\frac{K_z}{g} \frac{\partial P}{\partial z} - K_z(\rho - \rho_0) \tag{7}$$

where K_x, K_y, and K_z are the hydraulic conductivity (m/s), and ρ_0 is the referenced fluid density (kg/m^3). The dynamic pressure relative to the referenced hydrostatic pressure can be described as:

$$P = p + P_0 \tag{8}$$

where p is the gauge pressure [kg/(ms^2)].

The fluid properties like dynamic viscosity and density at an isothermal condition are given by the state laws:

$$\mu = \mu_0 \tag{9}$$

$$\rho = \rho_0[1 + \alpha S] \tag{10}$$

where μ_0 is the reference viscosity [kg/(ms)], α is a constant value (-), and S is the salinity (-).

2.1.2. Fracture Generation

DarcyTools uses the power-law size distribution for fracture generation, which can be written in terms of equivalent radius as follows:

$$f(r) = \frac{k_r r_0^{k_r}}{r^{k_r+1}},\ k_r \geq 2,\ r_0 < r < \infty \tag{11}$$

where r is the equivalent radius (m), k_r is the scaling characteristic of fractures as a function of size (-), and r_0 is the mathematical minimum radius (m) (the smallest fracture described by the power-law). The notation r_0 is the location factor and k_r is the shape factor. The scaling relationship of fracture intensity and fracture size is defined by the fracture surface area intensity, P_{32} $(r \geq r_1)$ (m^2/m^3), which is related to the intensity of all fractures larger than the minimum radius, P_{32} $(r \geq r_0)$ (m^2/m^3):

$$P_{32}(r \geq r_1) = P_{32}(r \geq r_1)\left(\frac{r_0}{r_1}\right)^{k_r-2} \tag{12}$$

where r_1 is the specific fracture radius (m). It is necessary to generate a truncated fracture size distribution $r_{min} \leq r \leq r_{max}$ (m) in reality. The intensity within the size interval is described as:

$$P_{32}(r_{min},\ r_{max}) = P_{32}(r \geq r_0)\left(\frac{r_{min}^{2-k_r} - r_{max}^{2-k_r}}{r_0^{2-k_r}}\right) \tag{13}$$

where r_{min} is the minimum fracture radius (m) and r_{max} is the maximum fracture radius (m). DarcyTools generates square-shaped fractures, so the length of equivalent fracture square is calculated as:

$$L = r\sqrt{\pi} \tag{14}$$

where L is the length of equivalent fracture square (m). The number of square-shaped fractures in a size range can be described as:

$$n = \left[\left(\frac{L + dL}{L_{ref}}\right)^{D} - \left(\frac{L}{L_{ref}}\right)^{D}\right]\frac{I}{D} \tag{15}$$

$$I = P_{32,tot}(k_r - 2)\frac{L^{k_r - 2}}{L_{ref}^{k_r}} \tag{16}$$

where n is the number of square-shaped fractures (-), and L_{ref} is the reference length of the square-shaped fracture (m). Notation I is the number of fractures per unit volume (-), and D is the negative value of the shaped factor (-). DarcyTools generates random fractures in space. This process is accomplished by utilizing independent uniform probability distributions for the location of fracture centers. The orientation of the fractures obeys the Fisher orientation distribution, where each fracture set is defined by mean pole trend, plunge, and concentration. The direction cosines of the generated fractures are defined as follows:

$$\lambda_1 = \cos(90 - tr)\cos(pl)\kappa \tag{17}$$

$$\lambda_2 = \sin(90 - tr)\cos(pl)\kappa \tag{18}$$

$$\lambda_3 = -\sin(pl)\kappa \tag{19}$$

where λ_1, λ_2, and λ_3 are the directions of the generated fractures (-), tr is the pole trend (-), pl is the pole plunge (-), and κ is the concentration parameter of fisher distribution (-).

2.1.3. Computational Grids and Representation of Fractures on a Grid

DarcyTools uses an unstructured adaptive Cartesian grid to avoid the generation of useless cells in regions of low interest. Starting from a single cell that covers the entire domain, the grid generator splits cells requiring refinement into two halves cells (i.e., 221 rule). It repeats this procedure for each direction until the cell size specification is reached. Then, cells outside the model domain are removed (including above the topography), and the remaining cells are assigned according to their characteristics or properties, e.g., cells inside DH, cells in the contact between DH and host rock, cells inside the deposition tunnel (DT). Structure and disposal facilities with different cell sizes can be defined from predefined objects such as lines, planes, and cylinders, but from triangulated shapers stored from CAD software using the Stereo Lithography (STL) file format.

DarcyTools is based on the finite volume method and generates the staggered grid. The different control volumes can be assigned the different variables according to the distribution of fractures and rock matrix within the different volumes. Directional properties are calculated on the faces between two adjacent grids. Anisotropy can be defined parallel to the three main directions on a Cartesian coordinate system. The scalar properties are calculated at the center of each control volume. If one takes hydraulic conductivity as an example, the concept for estimating the scalar and directional properties in a control volume is described as follows:

$$K_{cv} = \frac{T_f L_f W_f}{V_{cv}} \tag{20}$$

where K_{cv} is a control volume (m^3), and K_{cv} is the representative hydraulic conductivity for a control volume (m/s). Notation T_f is the transmissivity of an interesting fracture inside a control volume (m^2/s), L_f is the length of an intersecting fracture inside a control volume (m), and W_f is the width of an intersecting fracture inside a control volume (m).

If the control volume contains more than one fracture, each fracture will contribute to the representative value of the property for the control volume.

2.1.4. Particle Tracking Algorithms

DarcyTools uses the typical particle tracking algorithm, the traditional approach of moving the particle along the local velocity vectors, to simulate the transport in the numerical domain. In this study, we focus on advective transport, i.e., no chemical reactions, diffusion, or dispersion. Therefore, we ignore the influences of sorption, degradation, and decay on the transport processes. The movement of particles is predicted by integrating the trajectory equations for individual particles, using the instantaneous fluid velocity along the particle path. Once the flow fields are available, the solution to the first-order differential equation can employ classical numerical solvers such as Euler and Runge-Kutta methods. In the study, the Euler method yields the following formula:

$$X(t + \Delta t) = X(t) + V(x, t)\Delta t \tag{21}$$

where x is the particle location in space (m), t is the time (s), V is the seepage velocity in a particular location (m/s), and Δt is the specified time step (s) for the particle tracking. The calculations of the particle traces and the traveling times rely on accumulating the recorded particle locations at different time steps.

2.1.5. Performance Measures

In the KBS-3 disposal concept, containment and retardation are two critical issues throughout the assessment period. The understanding and evaluation of repository safety require a more detailed description of how the containment and retardation are maintained by the barriers, i.e., canister, buffer, backfill, and host rock. Among these barriers, the host rock should provide an acceptable hydrogeological and geochemical environment for the engineered barriers, limit fluid flow, and retard the migration of harmful substances that could be released from the repository [9–11,19–21]. Therefore, the host rock has critical functions in controlling the transport resistance in the buffer/rock interface and high resistance in the geosphere to limit the transport of solutes. In the quantitative evaluation of safety, it is desirable to express the functions to measurable or calculable quantities, called the safety function indicator. One of the safety functions of the host rock is to provide acceptable hydrogeological and transport conditions according to the KBS-3 disposal concept [9–11,19–21]., There are two indicators involved in evaluating the acceptable conditions. One indicator is the transport resistance in the buffer/rock interface, which is the equivalent flow rate (Q_{eq}) (m^3/s). Based on the KBS-3 disposal concept request, Q_{eq} in the buffer/rock interface below 1.0×10^{-4} m^3/year can be acceptable [20]. Another indicator is the resistance in the geosphere, which is the flow-related transport resistance (F) (s/m). Previous investigations have shown that the acceptable F value needs to be above 1.0×10^4 year/m for the flow paths from the repository to the biosphere [20]. The safety function indicator is to make the safety function measurable and calculable. Even if the hydrogeological conditions do not meet the criteria for the indicator of Q_{eq} and F, it does not mean the repository will be damaged or cause a considerable impact on the geosphere. However, the engineered barriers (i.e., the waste form, canister, buffer, and backfill) provide additional barriers that contain the waste and retard radionuclide transport, thus contributing to the performance of the total repository system [20]. In this study, we focus on Q_{eq} and F calculations. The comparisons between the calculation results and the indicator criteria will be conducted to evaluate the hydrogeological condition of the reference case.

In the KBS-3 disposal concept, radionuclides will leak out from the canister and migrate into the buffer material once the canister is damaged. One of the pathways is that radionuclides migrate into the mobile water in fractures surrounding the deposition hole (Q1 path) [9–11,19,20]. Figure 1 presents the schematic concept of the disposal facility and Q1 pathways for radionuclides to leave from the DH to the near field. Q_{eq} is for calculating the concentration of the compartments in contact with flowing water in a fracture in the rock. It is a fictitious flow rate of water that carries a concentration equal to that at the interface between buffer material and rock [28,29]. Q_{eq} depends on the geometry of the contact area, the water flux, and the diffusivity. For example, Q_{eq} for a fracture intersecting a DH is given by:

$$Q_{eq} = 2UW\sqrt{4D_w t_w/\pi} \quad (22)$$

where Q_{eq} is the equivalent flow rate (m^3/s), U is the equivalent initial flux in the fracture system averaged over the rock volume adjacent to the DH (m/s), W is the diameter of DH (m), D_w is the diffusion coefficient in free water (m^2/s), and t_w is the advective travel time (s), which is the time a water parcel is in contact with the compartment. In the process of calculating Q_{eq}, it is recognized as the DH volume. Otherwise, the advective travel time is defined as the time needed for a particle to traverse a cell of the total time of the particle movement from a start location to an end location.

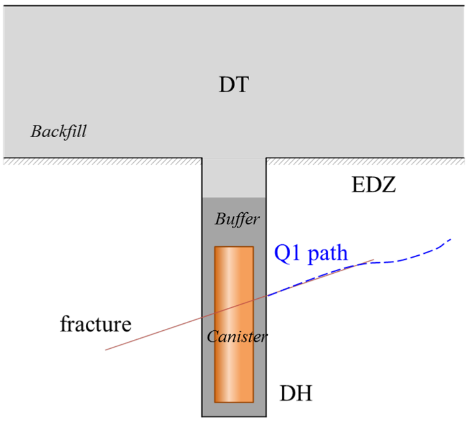

Figure 1. The schematic concept of the disposal facility and Q1 pathways for radionuclides to leave from the DH based on the KBS-3 disposal system. The fracture (in red color) interests the DH.

The particle tracking method is used to simulate the trajectory from DH to the biosphere [9–11,19]. For each particle trace, the flow path length (L) (m), advective travel time (t_w) (s), and F are calculated. The L values rely on adding the particle's travel path length through each computational cell. The advective travel time t_w accounts for the time needed for a particle to pass a cell or the total summation time of a particle as it moves from a start location to the end location. For safety assessment, F is an important parameter reflecting the transport resistance in the geosphere. The study estimates F along a flow path. In DarcyTools, F in each cell of the domain is represented as:

$$F = \left(\frac{a_r L}{q}\right)_i \quad (23)$$

where F is the flow-related transport resistance (s/m), a_r is the flow-wetted surface per volume of rock (m^2/m^3), L is the length of the cell (m), and q is the Darcy flux through the cell (m/s). The total F relies on the summation of piecewise F along the flow path of a particle. Note that all particles are only released at the fracture intersecting the DH with the highest flow rate (if multiple fractures intersect a DH). No particle will be released if a DH is without an intersection by any fracture. It is also noted that the additional release concept from the excavation damaged zone (EDZ) and DT can be of interest based on the releasing concept of the KBS-3 system. However, this study only considers the Q1 path.

2.2. Reference Case

There is no proposed candidate area or site for radioactive waste final disposal in Taiwan. To provide the researchers who can have the same fundamental information to iterate the technical ability, the reference case, which is a hypothetical platform, has been proposed. The essential geological data for the reference case is mainly based on the investigations and research of the eastern part of an offshore island of Taiwan [16]. We have translated coordinates for simulation purposes so that the coordinate is only for determining the domain size. In this section, we present the geometry of a conceptual disposal facility and then show the distribution of the main hydrogeological units of the reference case. The hydrogeological conceptual model includes the flow properties of hydrogeological units, the disposal facility, and the boundary conditions. Note that this study focuses on the flow and advective transport simulation in a numerical domain composed of fractured rock and a disposal facility. The detailed information about the investigation, experiment, in-situ tests, and the exact location for the reference case will not be presented and discussed here.

2.2.1. Conceptual Disposal Facility

We generate a basic disposal facility composed of the main tunnel (MT), DT, DH, and EDZ based on the concept of the KBS-3 system in this study. A complete disposal facility consists of the central area, shafts, ramps, and others. However, we only consider the primary disposal facility to be embedded in the numerical domain Q1 pathways and for the calculations of PMs. The geometry and location of MT, DT, DH, and EDZ are usually stored in the Stereo Lithography (STL) format and separated into four files, respectively. In this study, the basic disposal facility is assumed at a depth of 500 m and composed of two panels. Each panel contains an MT and 52 DTs. The length of the MT is 1000 m, and the length of DT is 250 m with 25 DHs capacity in the western panel, while the length of DT is 300 m with 30 DHs capacity in the eastern panel. The total number of the repository components contains two 1000 m long MT, 104 from 250 to 300 m long DTs, and 2860 DHs. Figure 2 shows the layout of a basic disposal facility. Figure 2a presents the plan view of the disposal facility. Figure 2b shows the MTs (in red color) and DTs (in green color) created by the four STL files. Figure 2c is the close view of parts of an MT (in red color), DTs (in green color), and DHs (in blue color). The diameter and height of each DH are 1.75 m and 8.155 m, respectively.

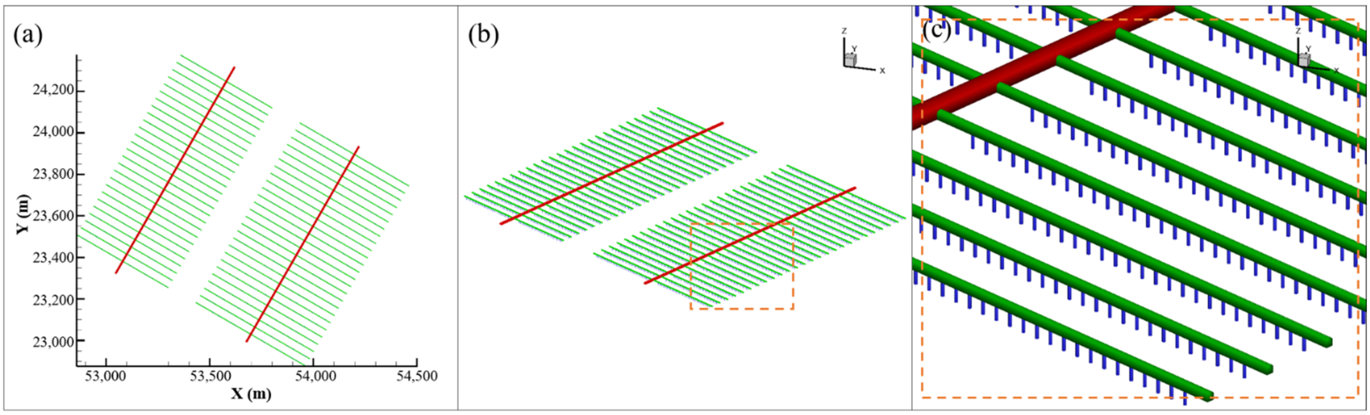

Figure 2. The basic disposal facility in this study. (**a**) The layout and location of the basic disposal facility are composed of two panels; (**b**) The design of MTs (in red color) and DTs (in green color). There are 2 MTs and 104 DTs; (**c**) The close view of parts of a MT (in red color), DTs (in green color), and DHs (in blue color). There are 2860 DHs in this conceptual disposal facility in this study.

2.2.2. Hydrogeological Conceptual Model

Figure 3 shows the hydrogeological conceptual model of the reference case. The length of the model domain is 30 km on the x- and y-axis, respectively (in Figure 3a), and the depth of the bottom boundary is −2000 m (in Figure 3c). The detail domain boundary is stored as a text file (XY file), and the surface topography as another text file (XYZ file). The model includes land and sea, and the salinity (3.2% for sea) is included in the model. The density of seawater is specified as 1.03 g/cm^3 [16]. The temperature is considered uniform so that there is no buoyancy due to the temperature variations. The lateral boundary condition is assigned as a specified hydrostatic pressure along the sea, and specified salinity is set as all lateral boundaries and at the bottom boundary. The bottom boundary is given as a no-flow boundary. The top boundary is assigned a specified recharge rate with fresh water of 68 mm/year [16]. In the model, the initial salinity condition is assigned as fresh water inside the island. Therefore, the fresh and saltwater interfaces are available based on the model simulations. Figure 3b presents the location and layout of a conceptual repository in the numerical domain.

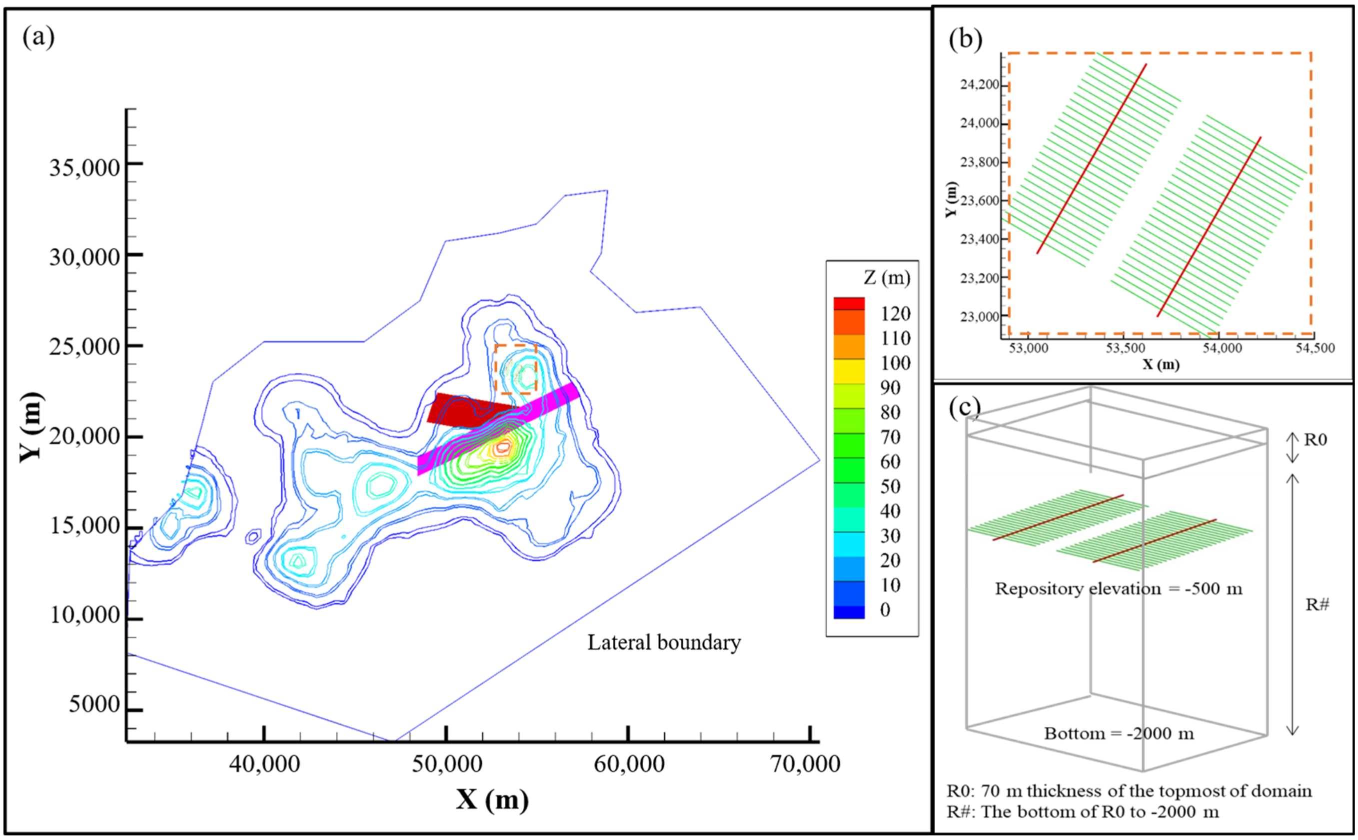

Figure 3. The hydrogeological conceptual model for the reference case: (**a**) The land and sea and the salinity (3.2% for sea) are considered in the model. There are two faults, including F1 (in pink) and F2 (in dark red), in the eastern area. The conceptual repository is in the northeast area of the simulation domain (marked with a dashed line); (**b**) The close view of the conceptual repository defined in (**a**); (**c**) The depth of the bottom boundary and the repository elevation.

The reference case is mainly composed of granitic gneiss, which is a kind of fractured rock, and there are two main water-conductive structures, fault (F1) and fracture zone (F2) within the area (in Figure 3a). The 70 m thickness of the topmost is assigned as the regolith (R0) based on the estimation of six borehole data for fracture intensity determination (in Figure 3c) [30–32]; whereas the remaining part is assigned as the rock domain (R#) which is composed of the fractures and rock matrix. Table 1 lists the distribution and flow properties of the hydrogeological units in the reference case. The range of hydraulic conductivity for R0 is from 5.0×10^{-6} to 1.0×10^{-4} m/s, and the recommended value is 1.0×10^{-5} m/s. The effective porosity of R0 is 1.0×10^{-3} (-). The range of hydraulic conductivity for R# is from 4.1×10^{-12} to 1.0×10^{-9} m/s, and the recommended value is 1.0×10^{-10} m/s. The effective porosity of R# is 5.4×10^{-3} (-). The attitude of F1 is N64E/70N, and its width is 200 m. The attitude of F2 is N80E/50S, and its width is 20 m. Note that F1 and F2 are constrained inside the eastern part of the island. Since there is no further information to prove the extent of F1 and F2 outside the island, we assume that F1 and F2 have limited lengths. The range of hydraulic conductivity for F#, i.e., F1 and F2, is from 3.0×10^{-8} to 1.0×10^{-4} m/s, and the recommended value is 5.0×10^{-6} m/s. The effective porosity of F1 is 1.0×10^{-2} (-), while the effective porosity of F2 is 1.5×10^{-2} (-). The hydrogeological conceptual model shall not be treated as a real site descriptive model representing the complete site understanding of a potential area or site [16,17].

The fractures are generated within R0 and R# domains based on the DFN recipe. The DFN recipe is composed of a series of fracture parameters in Table 2. We focus on DFN generation and the flow and advective transport simulation in the numerical domain composed of the fractured rock and a disposal facility. The detailed information about building up the DFN recipe can be referred to in previous studies [30–32]. The fractures are generated according to the Fisher distribution. Each fracture cluster is defined using pole trend, pole plunge, and concentration parameter of fisher distribution. There are four clusters in R0 and five clusters in R# based on the borehole fracture orientation analysis. The fracture intensity (P_{32}) is assumed as 2.4 and 0.3 for R0 and R#, respectively. The power-law shaper factor (k_r) of 2.6 is assigned for the fracture size distribution. The location parameter of minimum radius (r_0) is assigned as 0.1 m, and the minimum fracture radius (r_{min}) and maximum fracture radius (r_{max}) are 4.5 and 564 m, respectively. The spatial arrangement of the fracture center is assumed to be a stationary random (Poisson) process. The transmissivity of fracture is a function of fracture size based on the empirical function from the Swedish Forsmark site [18]. The fracture aperture is the function of fracture transmissivity.

Table 1 also lists the flow properties of the components of the disposal facility. The hydraulic conductivity is 1.0×10^{-10} m/s for MT and DT to represent the flow properties of backfill material, while the hydraulic conductivity is 1.0×10^{-12} m/s inside DH to represent the property of buffer material [33]. A canister should be in the DH center based on the formal KBS-3 disposal concept. Here, we ignore the canister and assume each DH is all deposited by buffer material. In addition, according to the studies, the width of EDZ is around 30 cm, and the transmissivity varies from 1.0×10^{-9} to 1.0×10^{-7} m^2/s [34]. Therefore, the recommended transmissivity for EDZ is 1.0×10^{-8} m^2/s, and the porosity is 1.0×10^{-4} (-). We directly calculate the hydraulic conductivity of EDZ according to transmissivity and width of EDZ. The hydraulic conductivity of EDZ is 3.3×10^{-8} m/s based on the transmissivity divided by the width.

Table 1. The flow properties of hydrogeological units and EDZ for the conceptual model in this study.

Units	Lithology or Material	Distributions/Attitude and Width	Range of Hydraulic Conductivity (m/s)	Recommended Hydraulic Conductivity (m/s)	Porosity (-)
R0	Regolith	70 m thickness of the topmost domain	5.0×10^{-6}–1.0×10^{-4}	1.0×10^{-5}	1.0×10^{-3}
R#	Granitic gneiss	-	4.1×10^{-12}–1.0×10^{-9}	1.0×10^{-10}	5.4×10^{-3}
F1	Fault	N64E/70N, 200 m width	3.0×10^{-8}–1.0×10^{-4}	5.0×10^{-6}	1.0×10^{-2}
F2	Fracture zone	N80E/50S, 20 m width	3.0×10^{-8}–1.0×10^{-4}	5.0×10^{-6}	1.5×10^{-2}
MT	Backfill material	-	-	1.0×10^{-10}	4.0×10^{-1}
DT	Backfill material	-	-	1.0×10^{-10}	4.0×10^{-1}
DH	Buffer material	-	-	1.0×10^{-12}	4.0×10^{-1}
EDZ	Granitic gneiss	-	3.3×10^{-9}–3.3×10^{-7}	3.3×10^{-8} *	1.0×10^{-4}

* The recommended transmissivity of EDZ is 1.0×10^{-8} m^2/s [34]. The width of EDZ is around 30 cm, so the hydraulic conductivity is calculated via the transmissivity divided by the width.

Table 2. The DFN recipe for R0 and R#.

Fracture Domain		**R0**	**R#**
Elevation		Depth below surface < 70 m	Depth below surface > 70 m
Fracture clusters (Pole trend, pole plunge, κ, $P_{32,\,rel}$)	Cluster 1	(198, 18, 18, 26%)	(65, 17, 20, 15%)
	Cluster 2	(155, 4, 15, 24%)	(344, 38, 18, 24%)
	Cluster 3	(264, 23, 16, 18%)	(281, 29, 16, 30%)
	Cluster 4	(98, 81, 11, 32%)	(174, 22, 17, 10%)
	Cluster 5	-	(175, 75, 19, 21%)
Fracture intensity(P_{32})		2.4	0.3
Fracture size		Power law : $k_r = 2.6$, $r_0 = 0.1$ m, $r_{min} = 4.5$ m, $r_{max} = 564$ m	Power law : $k_r = 2.6$, $r_0 = 0.1$ m, $r_{min} = 4.5$ m, $r_{max} = 564$ m
Fracture location		Stationary random (Poisson) process	Stationary random (Poisson) process
Fracture transmissivity (T, m^2/s)		$T = 1.51 \times 10^{-7} \times (L^{0.7})$; $L = \sqrt{(\pi r^2)}$ L is the equivalent size (m) of a square fracture.	$T = 3.98 \times 10^{-10} \times \left(L^{0.5}\right)$; $L = \sqrt{(\pi r^2)}$ L is the equivalent size (m) of a square fracture.
Fracture Aperture (e, m)		$e = 0.5\sqrt{T}$	$e = 0.5\sqrt{T}$

3. Numerical Examples

3.1. Workflow for the Study

There are three main tasks in this study. One is the flow and advective transport simulation and PMs calculation for the base case. Since the recommended flow properties are determined for each hydrogeological unit, it is necessary to simulate the flow and transport as a basis for this reference case. The second task is the sensitivity analysis of flow properties in the hydrogeological units and EDZ, and the third one is the uncertainty analysis of collected DFN realizations. More specifically, in the first task, we model the flow and advective transport based on the conceptual model and the associated recommended flow properties for hydrogeological units. Then, we calculate the PMs based on the flow and advective transport results. For the second task, we focus on adjusting the hydraulic conductivity of each hydrogeological unit (i.e., R0, R#, F#) and EDZ and estimating its influence on the calculations for PMs. Table 1 lists the range of hydraulic conductivity for four hydrogeological units, and the upper and lower bound of hydraulic conductivity are selected as the sensitivity cases. There are eight cases, based on calculating four hydrogeological units for two bounding hydraulic conductivities. For the third task, we focus on generating a series of additional DFNs and estimating their influence on the calculations for PMs. We generated additional 48 realizations and involved the stochastic modeling concept to analyze the distribution of the realizations systematically.

There are various steps included in the workflow for this study (see Figure 4). The main steps in the first task are the computational grid generation, DFN generation, fracture connectivity analysis, intersected DH calculations after applications of rejection criteria, effective hydraulic property transformation, flow simulation, particle tracking simulation, and then the PMs calculation. First, we check the geometry and distribution of the hydrogeological conceptual model (in Figure 3) and create the objects for the following computational grid generation. We then generate an example DFN based on the DFN recipe (in Table 2), and the fracture connectivity analysis is conducted to maintain the connected fracture system. The connected fracture system is up-scaled to the specific effective hydraulic conductivity in each cell based on the concept of the ECPM model. The flow field is then simulated based on the boundary condition in Figure 3. Q_{eq} for each DH can be calculated based on the head distribution and the results of intersected DH calculations after applications of rejection criteria. In addition, the intersected DH calculations also provide the start location for the particle tracking simulation. The particle tracking method can record the particle locations on the cell in each step and the total length and time accumulate the step-by-step distance and time from a start location to the end location. Finally, the trace information, including L, $t_{w,}$ and F, is calculated by abstracting the flow path data.

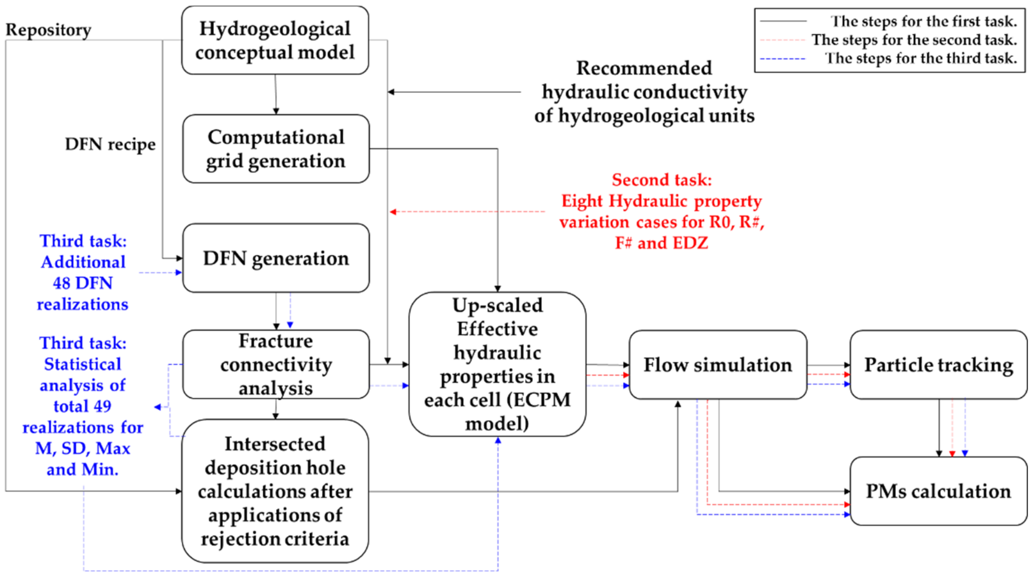

Figure 4. The main steps involved in the workflow are to simulate flow and advective transport and calculate the PMs for three tasks in this study.

The study employs the generated computational grids and adjusts the hydraulic conductivity of each hydrogeological unit for R0, R# and F#, and EDZ. The study uses the same computational grid and the example DFN but changes the hydraulic conductivity for hydrogeological units and EDZ once a time based on the upper and lower bound of hydraulic conductivity shown in Table 1 (marked with red text in Figure 4). Eight cases are simulated for the flow and advective transport based on the same boundary condition assigned in the base case, and the PMs for each case are calculated. For the third task, additional 48 realizations of DFN are generated and up-scaled to be the effective flow properties in each grid. The third task uses the same computational grid but generates additional 48 realizations for the simulations. For each realization, the model conducts the fracture connectivity analysis, the intersected DH calculations based on rejection criteria, and the up-scaled effective flow properties (marked with blue text in Figure 4). We employ the stochastic modeling concept to analyze the effective fracture number and the number of the potential canister failure induced by DH rejection criteria for the one example DFN and additional 48 realizations, i.e., a total of 49 realizations. The mean (M), standard deviation (SD), maximum (Max), and minimum (Min) values are analyzed (in blue color). We then choose the realizations related to the statistics to simulate the flow and advective transport and calculate the PMs based on the same boundary condition assigned in the base case.

In summary, this study aims to assess the flow and advective transport based on the hydrogeological conceptual model of the reference case. The computational grid and boundary conditions are the same for all three proposed tasks. In the sensitivity analysis, the study varies the hydraulic conductivity for each hydrogeological unit and EDZ. Simulation results are the basis for quantifying the influence of hydraulic conductivity variations on flow and advective transport. The additional 48 realizations of DFNs are for the uncertainty analysis of flow and advective transport in the study.

3.2. DFN Generation, Fracture Connectivity Analysis, and Intersections between Fractures and Repository

The DFN generation and fracture connectivity are critical issues for flow and transport dynamics in fractured rock. In addition, the intersections between fractures and the disposal facility dominate the detailed flow in the repository area and the PMs in the near-field. The fracture connectivity controls the regional flow field and advective transport in the numerical domain. Figure 5 presents an example of DFN realization using the DFN recipe shown in Table 2 and the associated geometry of the repository. Figure 5a shows the connected (in light blue color) and isolated (in orange color) fractures in contact with the repository. Figure 5b is a close view of the repository. DarcyTools focuses on flow in the connected fracture to the disposal facility since only the connected fracture is potentially providing the flow paths. The fracture connectivity analysis removes all isolated fractures before calculating the up-scaled hydraulic conductivity for all the computational grids.

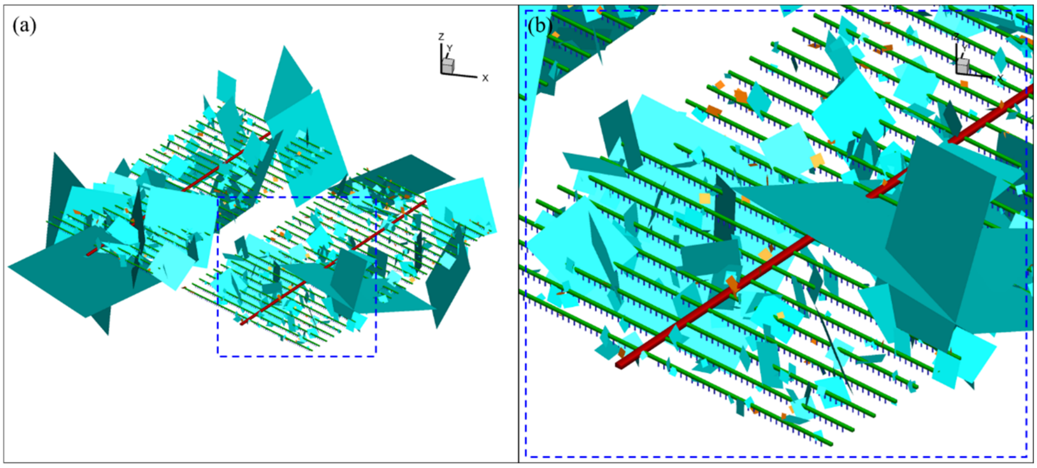

Figure 5. The example DFN realization using the DFN recipe and the repository. (**a**) The fractures that intersect the repository are divided into connected (in light blue color) and isolated fractures (in orange color). It is also noted that colors are influenced by light and shade; (**b**) The close view of the MT (in red color), DT (in green color), the connected fractures (in light blue color), and isolated fractures (in orange color).

In this study, all DH locations are evaluated based on DH rejection criteria, which examines the intersection of a DH by a fracture and conservatively assumes shear failure of the canister caused by fractures. There are two DH rejection criteria, including (1) full perimeter criterion (FPC) and (2) extended full perimeter criterion (EFPC). Figure 6 shows the schematic concept of the geometric DH rejection criteria for FPC and ECPC. FPC states that if a fracture intersects the full perimeter of the DT, and the hypothetical extension of the fracture would intersect a DH, the DH is rejected (in Figure 6a). EFPC states that if a fracture intersects one DH and also intersects four or more adjacent DHs, these five or more DHs are to be rejected (in Figure 6b). We involve the DH rejection criteria to calculate the number of rejected and remaining DHs. Based on Figure 5, the numbers of DHs intersected by connected and isolated fractures are listed in Table 3. In addition, the number of DHs for connected fractures can be divided into the rejected and the remaining DH numbers. There are three potential release paths from the canister. The Q1 path is the dominant one for the dose calculation in this study. Therefore, the simulations of release paths focus on the Q1 paths.

Table 3 illustrates an example to show the intersection detected based on the realization of the base case, i.e., the results in Figure 5. Figure 5a shows the view of fractures near the repository. Figure 5b is a close view of the MT (in red color), DT (in green color), the connected fractures (in light blue color), and isolated fractures (in orange color). In the demonstrated realization, there are 365 DHs intersected by the connected fractures and

47 DHs intersected by the isolated fractures. Table 3 presents the number of remaining DHs after applying the rejection criteria. The remaining DHs are 148, the target for particle tracking simulation and PMs calculation. In the study, we generate additional 48 DFN realizations based on the same DFN recipe listed in Table 2. Therefore, the DHs intersected by connected and isolated fractures must be calculated based on the 48 DFN realizations. Besides, the effective fracture number (i.e., the number of connected fractures) for each realization is calculated for the stochastic analysis.

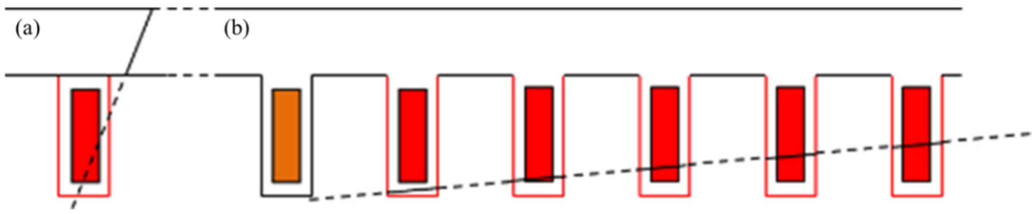

Figure 6. The schematic representation of the geometric DH rejection criteria. Canisters shown in red color indicate the rejected DHs. (**a**) A deposition hole position was rejected due to FPC prior to drilling; (**b**) Five deposition positions intersected by a fracture intersecting in a row are rejected.

Table 3. The numbers of DHs obtained from the intersected fractures in the example DFN.

Number of DH Intersected by Isolated Fractures	Number of DH Intersected by Connected Fractures	Number of DH with Rejection Criteria	Remained Number of DH for Q1 Path
47	365	217	148

3.3. The Computational Grid and Effective Flow Properties Field for the Base Case

In this study, the domains for R0, R#, and F# and the disposal facility components are stored as the STL file, and DarcyTools can directly read the files and assign the cell size for each structure and object. The cell refinement is applied from the default cell size of 256 m × 256 m × 256 m by setting a small cell size of 32 m × 32 m × 32 m in the F1 and F2. The cell size on the top of the domain is 32 m × 32 m × 2 m. The spatial refinement in the z-direction is to fit the detailed variations of the topography. The grid is globally refined in the repository zone with a cell size of 8 m × 8 m × 8 m. Smaller cell sizes are generated near the tunnels (1 m × 1 m × 1 m), EDZ (0.25 m × 0.25 m × 0.25 m), and DH (0.125 m × 0.125 m × 0.125 m) to capture the flow near the DH and the advective transport pattern close to the repository. The successive refinement leads to a total of 11,613,681 cells in the study (see Figure 7). Figure 7a shows the horizontal plane of the grids at z = −504 m, i.e., the center of gravity of DH. The cell size in F1, F2, and repository zone have been refined accordingly. Figure 7b presents the zoom-in view on F1, F2, and the repository zone of the horizontal cut at z = −504 m. Figure 7c is the close view of the refinement grids for the repository on the plane of z = −504 m. Figure 7d further shows the region for the DTs and DHs on the horizontal plane at z = −504 m. Figure 7e shows a vertical profile along x = 56,265, a vertical plane across the repository. Figure 7f is the profile view of the generated grids for an MT and DTs along x = 56,265.

The next step is to upscale the flow properties of fractures and rock matrix to become the effective flow properties in each grid. Figure 8 demonstrates the resulting hydraulic conductivity fields of the example realization for the base case. In Figure 8, the up-scaled hydraulic conductivity values are on the plane of z = −504 m. The hydraulic conductivity of F1 and F2 are assigned as the constant value of 5.0×10^{-6} m/s based on the hydrogeological conceptual model. The up-scale hydraulic conductivity varies from 1.0×10^{-9} to 1.0×10^{-10} m/s in R#, which meets the original range from the results of the field hydraulic test and laboratory experiments. A similar strategy is applied to the case of R0.

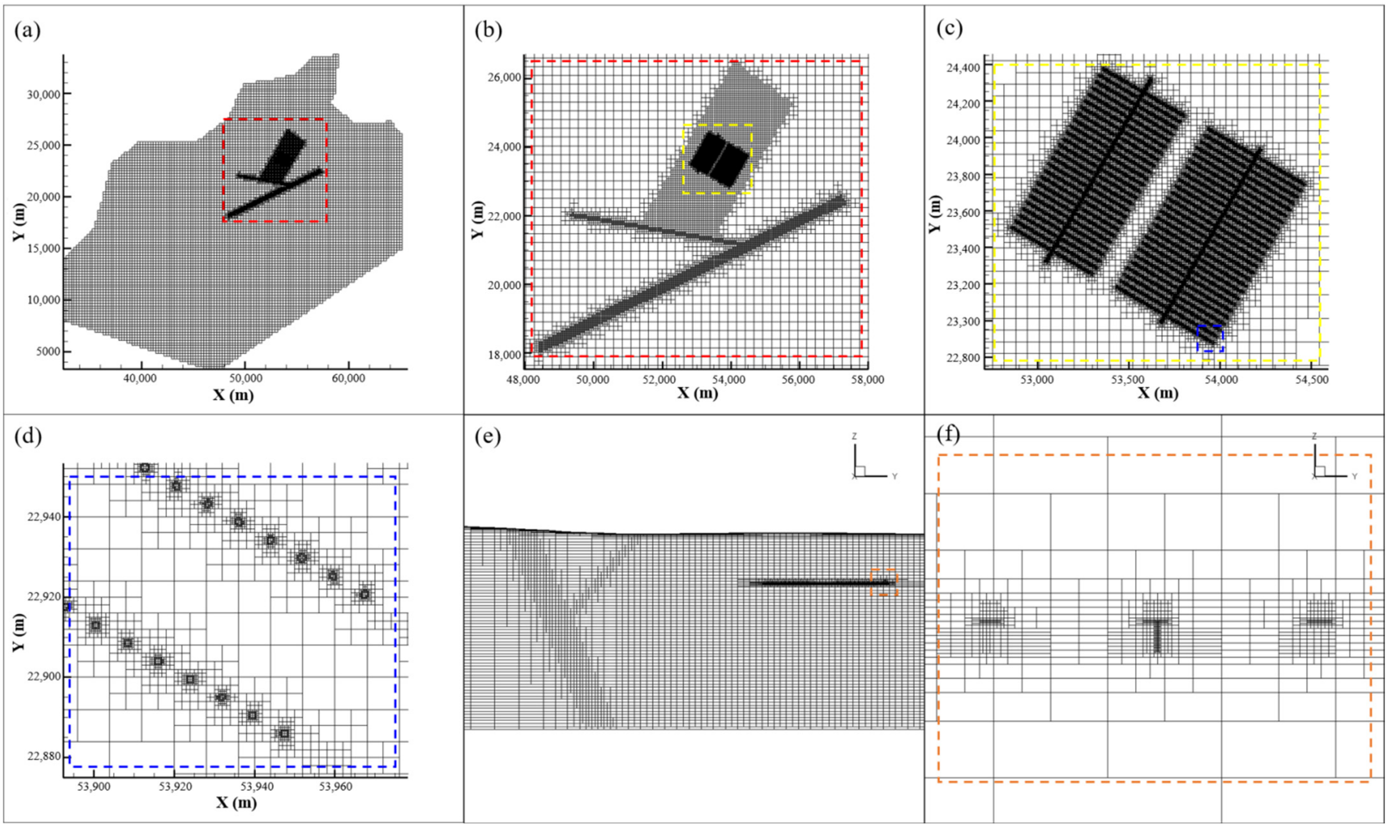

Figure 7. The computational grid in this study. (**a**) The horizontal plane view of the grids on the plane of z = −504 m; (**b**) The zoom-in view of girds for F1, F2, and repository zones based on the selected local area (red dashed line) shown in (**a**); (**c**) The refined grids for the repository area based on the selected local area (yellow dashed line) defined in (**b**); (**d**) The further zoom-in view of the DTs and DHs on the plane of z = −504 m. The local area is marked with the blue dashed line in (**c**); (**e**) The vertical profile of grids along x = 56,265; and (**f**) The close view of the refine grids for an MT and DTs in the area marked with the orange dashed line defined in (**e**).

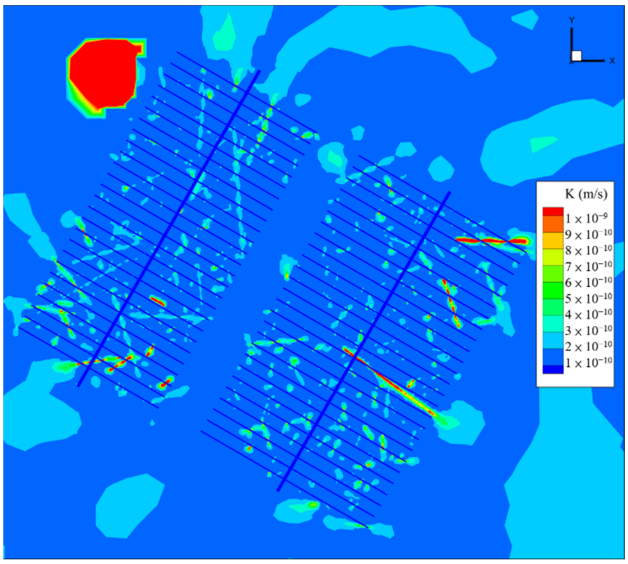

Figure 8. The plan view of the effective hydraulic conductivity based on the example DFN in the repository area.

4. Results and Discussions

This section focuses on presenting the results based on the specified steps defined in the workflow. The base case uses the hydrogeological conceptual model derived from the reference case in Taiwan and an example DFN generated according to the site-specific DFN recipe. The sensitivity analysis considers the steady-state groundwater flow and the associated particle traces for the PMs. An additional 48 DFN realizations are employed to conduct the uncertainty analysis. We focus on the Q1 path for all the assessments of the PMs.

4.1. Steady-State Flow, Particle Tracking, and Calculation of PMs for the Base Case

Figure 9 shows the dynamic pressure, salinity, and Q1 paths of the base case. Figure 9a presents the dynamic pressure distribution and Q1 paths on the repository depth and in two vertical profiles across the center of the repository. Figure 9b shows the salinity field and Q1 paths on the repository level and two vertical profiles across the center of the repository. The pressure results show that the central area is likely to be higher, and the pressure decreases gradually from the center to the coastal line. The result indicates that the groundwater could flow from the central area to the coastline. The salinity result shows a clear seawater and freshwater interface beneath the island, and flow paths would be affected accordingly. Based on the groundwater flow field results, we use the particle tracking method to model potential release Q1 paths. The particle release number is highly related to repository layout, fracture system, and geometrical rejection criteria. According to the setting of these parameters, the results show a total of 148 potential release locations for the Q1 paths. The results indicate that the paths are strongly influenced by groundwater flow and salinity fields. The results also show that particles tend to move toward the north, the northeast, and the northwest due to the relatively high groundwater potential in the central area. The seawater and freshwater interface will also influence flow paths near the coastal area. That is, the downward flow paths turn upward at the interface, leading to most of the particles discharged near the coastal line.

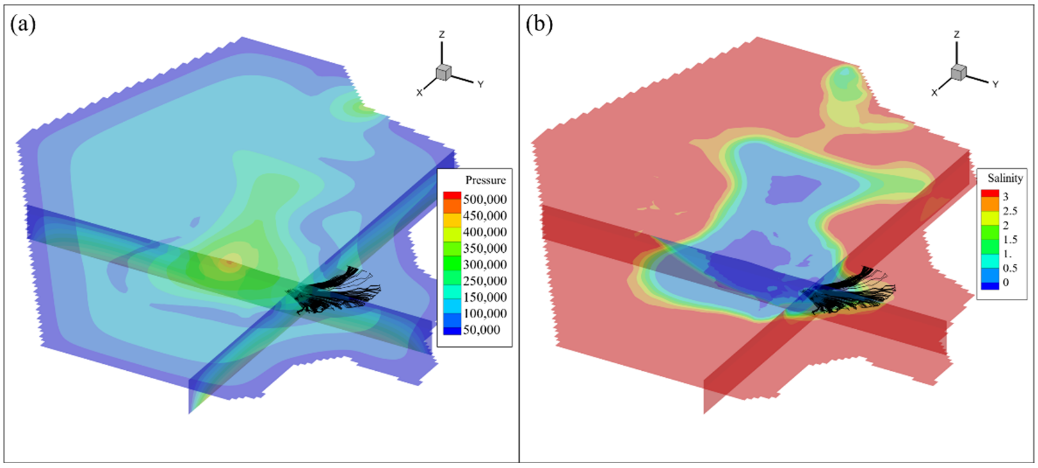

Figure 9. The steady-state flow, salinity field, and Q1 paths in the base case. (**a**) The pressure distribution and Q1 paths on the repository depth and two vertical profiles across the center of the repository. (**b**) The salinity field and Q1 paths on the repository depth and two selected profiles across the center of the repository.

Figure 10 shows Q_{eq} and F for Q1 paths in the base case. Figure 10a is the cumulative distribution function (CDF) of Q_{eq}; while Figure 10b is the CDF of F. Figure 10a indicates that the maximum value of Q_{eq} is 8.72×10^{-5} m^3/year, which fulfills the requirements of safety function indicator (i.e., smaller than 1.0×10^{-4} m^3/year). The minimum value of Q_{eq} is 4.55×10^{-5} m^3/year. The maximum value is higher than the minimum value of 1.92 times. The result indicates a stable flow field in the repository area. Figure 10b shows that the minimum value of F is 2.51 × 10^6 year/m, which fulfills the requirements of the safety function indicator (i.e., higher than 1.0 × 10^4 year/m). The maximum value of F is 4.78 × 10^7 year/m. The maximum value is higher than the minimum value by 19.01 times. The high variations are between the fraction of 0 to 20%, but the curve becomes smooth when F is higher than 1.16 × 10^7 year/m.

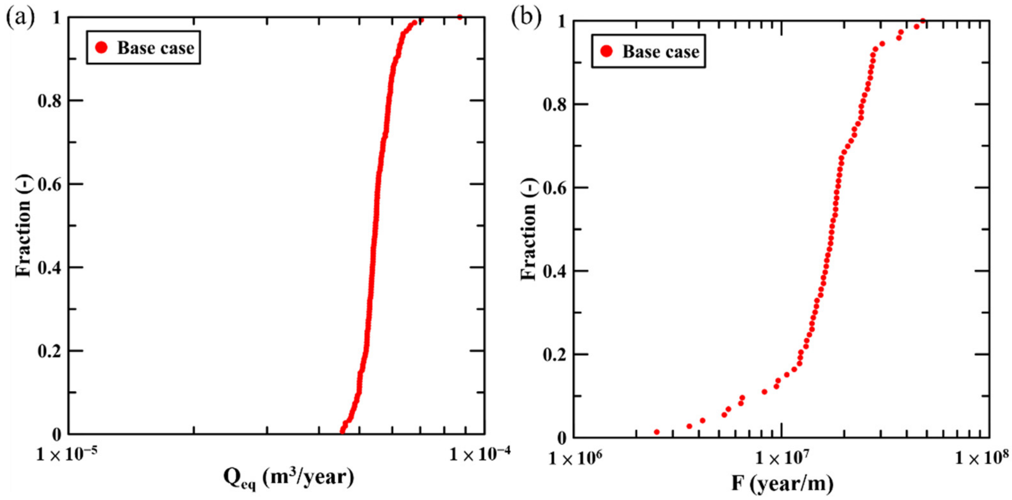

Figure 10. Q_{eq} and F for the Q1 path in the base case. (**a**) The Q_{eq} for the Q1 path of the base case; (**b**) The F for the Q1 path of the base case.

4.2. Sensitivity of Hydrogeological Units and EDZ on Flow, Particle Tracking, and PMs

Figure 11 shows the plane and profile views for the steady-state flow and particle traces. Figure 11a presents the base case results, i.e., the same results as described in Figure 9a. We use the base case as the basis for the qualitative comparisons between the base case and hydraulic conductivity sensitivity cases. Figure 11b,c are the hydraulic conductivity sensitivity cases for R0, i.e., the regolith. Figure 11b shows the hydraulic conductivity decreases to 5.0 × 10^{-6} m/s, and Figure 11c presents the hydraulic conductivity increases to 1.0 × 10^{-4} m/s. Figure 11d,e are the hydraulic conductivity sensitivity cases for R#, i.e., the host rock. Figure 11d shows the hydraulic conductivity decreases to 1.0 × 10^{-12} m/s, and Figure 11e presents the hydraulic conductivity increases to 1.0 × 10^{-9} m/s. Figure 11f,g are the hydraulic conductivity sensitivity cases for F#, i.e., the fault and fracture zones. Figure 11f shows the hydraulic conductivity decreases to 1.0 × 10^{-8} m/s. Figure 11g presents the hydraulic conductivity increases to 1.0 × 10^{-4} m/s. Figure 11h,i are the hydraulic conductivity sensitivity cases for EDZ. Figure 11h shows the case with hydraulic conductivity decreasing to 3.3 × 10^{-9} m/s. Figure 11i results display the hydraulic conductivity increasing to 3.3 × 10^{-7} m/s.

Figure 12 shows the CDF of Q_{eq} and F for cases of hydraulic conductivity sensitivity study. Figure 12a shows Q_{eq} of the hydraulic conductivity sensitivity cases. For R0 cases, the decrease of hydraulic conductivity of R0 (i.e., R0_5.0 × 10^{-6} m/s) makes all of Q_{eq} larger than those obtained from the base case by 1.03 times. The minimum Q_{eq} is 4.69 × 10^{-5} m^3/year, while the most significant value is 9.01 × 10^{-5} m^3/year. The result indicates that the lower hydraulic conductivity for R0 has no considerable impact on Q_{eq}. On the other hand, the increased hydraulic conductivity of R0 (i.e., R0_1.0 × 10^{-4} m/s) makes all of Q_{eq} lower than those obtained from the base case from 1.43 to 3.45 times. The minimum Q_{eq} is 1.32 × 10^{-5} m^3/year, while the maximum value is 6.08 × 10^{-5} m^3/year. The result indicates that the higher hydraulic conductivity for R0 could lead to a higher flow rate from the top boundary to the repository depth than those of the base case. This behavior makes the Q_{eq} values higher than those obtained from the base case. In addition, the deviation between the smallest and largest values is 4.61 times greater than that in the base case.

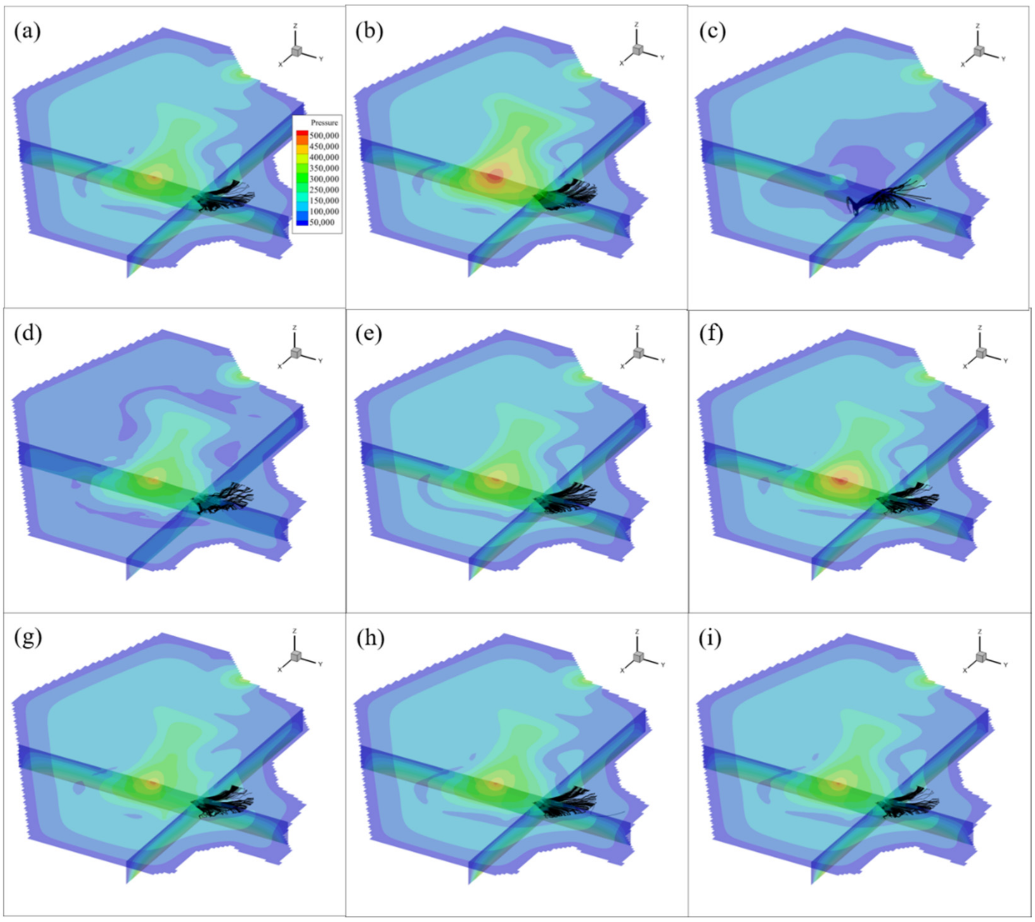

Figure 11. The steady-state flow fields for cases of hydraulic conductivity sensitivity analyses. The selected horizontal planes for the plots are on the repository depth, and two vertical profiles are defined across the center of the repository. (**a**) The base case; (**b**) The hydraulic conductivity of R0 decreases to 5.0×10^{-6} m/s; (**c**) The hydraulic conductivity of R0 increases to 1.0×10^{-4} m/s; (**d**) The hydraulic conductivity of R# decreases to 1.0×10^{-12} m/s; (**e**) The hydraulic conductivity of R# increases to 1.0×10^{-9} m/s; (**f**) The hydraulic conductivity of F# decreases to 1.0×10^{-8} m/s; (**g**) The hydraulic conductivity of F# increases to 1.0×10^{-4} m/s. (**h**) The hydraulic conductivity of EDZ decreases to 3.3×10^{-9} m/s; and (**i**) The hydraulic conductivity of EDZ increases to 3.3×10^{-7} m/s.

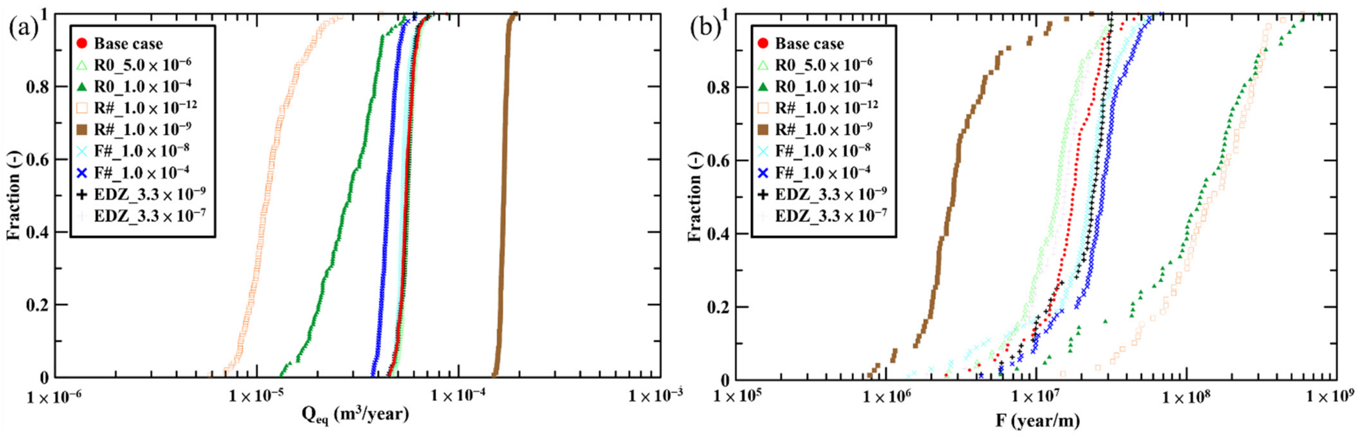

Figure 12. Q_{eq} and F for the Q1 paths in the cases for sensitivity analyses. (**a**) The Q_{eq} for the Q1 path of the sensitivity study cases. (**b**) The F for the Q1 path of sensitivity study cases.

For R# cases, the decrease of hydraulic conductivity of R# (i.e., R#_1.0 $\times$ 10^{-12} m/s) makes all of Q_{eq} smaller than those obtained from the base case. The minimum Q_{eq} is 5.88 $\times$ 10^{-6} m^3/year, while the maximum value is 4.12 $\times$ 10^{-5} m^3/year. The result indicates that the lower hydraulic conductivity for R# considerably decreases the flow rate in the repository region. On the other hand, the increased hydraulic conductivity of R# (i.e., R#_1.0 $\times$ 10^{-9} m/s) leads all of Q_{eq} to be higher than those obtained from the base case from 2.19 to 3.28 times. The minimum Q_{eq} is 1.49 $\times$ 10^{-4} m^3/year, while the maximum value is 1.91 $\times$ 10^{-4} m^3/year. The result indicates that the higher hydraulic conductivity for R# could lead to a higher flow rate in the repository region. Specifically, all values are more significant than the safety function indicator for the acceptable hydrogeological condition in the geosphere (i.e., smaller than 1.0 $\times$ 10^{-4} m^3/year).

For the F# cases, whether the hydraulic conductivity for F# is lower or higher than the value of the base case (i.e., 5.0 $\times$ 10^{-6} m/s), most Q_{eq} values are lower than those of the base case. When the hydraulic conductivity of F# is lower than the base case value, the minimum Q_{eq} is 4.55 $\times$ 10^{-5} m^3/year, while the maximum value is 7.39 $\times$ 10^{-5} m^3/year. The result indicates a behavior similar to that in the base case. When the hydraulic conductivity is larger than the recommended value, the lowest Q_{eq} is 3.76 $\times$ 10^{-5} m^3/year, while the highest value is 6.07 $\times$ 10^{-5} m^3/year. The result indicates that the increased hydraulic conductivity of F# makes all Q_{eq} smaller than those obtained from the base case, varying from 1.21 to 1.44 times. The flow field in the repository region is toward the north, northeast, and northwest, according to the top boundary and terrain. Further, the repository is far from the F#, and the influence might not be significant once the hydraulic conductivity for F# is changed.

For EDZ cases, whether the hydraulic conductivity for EDZ is lower or higher than the value of the base case (i.e., 3.3 $\times$ 10^{-8} m/s), all Q_{eq} are similar to those obtained from the base case. When the hydraulic conductivity of EDZ is lower than the base case value, the minimum Q_{eq} is 4.62 $\times$ 10^{-5} m^3/year, while the maximum value is 7.67 $\times$ 10^{-5} m^3/year. The result indicates a minor influence of the EDZ hydraulic conductivity on the flow. When the hydraulic conductivity is larger than the value of the base case, the minimum Q_{eq} is 4.48 $\times$ 10^{-5} m^3/year, while the maximum value is 7.53 $\times$ 10^{-5} m^3/year. The result shows that the increase of hydraulic conductivity of EDZ makes all Q_{eq} similar to those obtained from the base case. Note that the discussion only focuses on Q_{eq} for the Q1 path. Once the target switches to another releasing path based on the KBS-3 disposal concept, Q_{eq} results might be different.

Figure 12b shows F for the hydraulic conductivity sensitivity cases. For R0 cases, the decrease of hydraulic conductivity of R0 (i.e., R0_5.0 $\times$ 10^{-6} m/s) makes most of F slightly smaller than those obtained from the base case up to 1.43 times. However, only the minimum F (2.54 $\times$ 10^6 year/m) is slightly larger than the base case at 1.01 times. The maximum value (6.15 $\times$ 10^7 year/m) is higher than that obtained from the base case up to 1.29 times. The result indicates that the lower hydraulic conductivity for R0 has less impact on F. On the other hand, the increased hydraulic conductivity of R0 (i.e., R0_1.0 $\times$ 10^{-4} m/s) makes F larger than those obtained from the base case, and the values vary from 2.30 to 15.92 times as compared to those obtained from the base case. The minimum F is 5.78 $\times$ 10^6 year/m, while the maximum value is 7.61 $\times$ 10^8 m^3/year. The result indicates that the higher hydraulic conductivity for R0 might lead to a higher flow rate from the top boundary to the repository depth. The behavior reduces the particle transport velocity from the repository to the top of the model domain. In addition, the deviation between the smallest and largest values is 131.60 times, reflecting the high variations between the traveling traces of particles.

For R# cases, the decrease of hydraulic conductivity of R# (i.e., R#_1.0 $\times$ 10^{-12} m/s) makes F larger than those obtained from the base case, and the differences vary from 6.00 to 12.37 times. The minimum F is 1.51 $\times$ 10^7 year/m, while the maximum value is 5.91 $\times$ 10^8 year/m. The result indicates that the lower hydraulic conductivity for R# considerably decreases the flow rate in the entire numerical domain. It causes a lower travel velocity for each particle and makes considerable deviations in the particle traces. The increased hydraulic conductivity of R# (i.e., R#_1.0 $\times$ 10^{-9} m/s) leads to F values smaller than those obtained from the base case, and the differences vary from 2.05 to 3.24 times. The minimum F is 7.77 $\times$ 10^5 year/m, while the most significant value is 2.33 $\times$ 10^7 year/m. The result indicates that the higher hydraulic conductivity for R# makes the flow rate higher than that obtained from the base case. The relatively high flow rate could reduce the transport time for each particle from the repository to the biosphere. Although all the values are higher than the safety function indicator for the acceptable hydrogeological condition in the geosphere (i.e., higher than 1.0 $\times$ 10^4 year/m), several values are smaller than the 1.0 $\times$ 10^6 year/m, which is relatively low compared to the other cases in this study.

For F# cases, whether the hydraulic conductivity for F# is higher or lower than the value of the base case (i.e., 5.0 $\times$ 10^{-6} m/s), most F values are higher than those obtained from the base case. When the hydraulic conductivity of F# is lower than the value of the base case, the minimum F is 1.41 $\times$ 10^6 year/m, while the largest value is 6.17 $\times$ 10^7 year/m. The result indicates that 20% of F values are slightly smaller than those in the base case, while 80% of F values are slightly larger than those in the base case. When the hydraulic conductivity of F# is larger than the value of the base case, the minimum F is 4.29 $\times$ 10^6 year/m, while the maximum value is 6.83 $\times$ 10^7 year/m. The result indicates that the increased hydraulic conductivity of F# makes F slightly larger than those obtained from the base case, and the differences vary from 1.43 to 1.71 times for 80% of F values. The result could be that the flow field in the repository region is toward the north, northeast, and northwest, according to the top boundary and terrain. Besides, the repository is far from the F#. Therefore, the influence might not be significant when the hydraulic conductivity for F# is changed.

For EDZ cases, whether the hydraulic conductivity for EDZ is lower or higher than the value of the base case (i.e., 3.3 $\times$ 10^{-8} m/s), most F values are very similar to those obtained from the base case. When the hydraulic conductivity of EDZ is lower than the value of the base case, the minimum F is 2.24 $\times$ 10^6 year/m, while the most significant value is 5.33 $\times$ 10^7 year/m. The result indicates that 60% of F values between fractions from 25% to 95% are slightly smaller than those of the base case, while 25% of F values between fractions from 0% to 25% are very similar to those of the base case. When the hydraulic conductivity of EDZ is higher than that of the base case, the minimum F is 1.88 $\times$ 10^6 year/m, while the maximum value is 5.29 $\times$ 10^7 year/m. The result shows that the increased hydraulic conductivity of EDZ makes F values slightly smaller than those obtained from the base case, but the maximum value is higher than those obtained from the base case.

This study evaluated the sensitivity induced by the hydraulic conductivity variations for the hydrogeological units (including R0, R#, F#) and EDZ. Table 4 lists the maximum and minimum values of Q_{eq} and F for the base case and cases with hydraulic conductivity sensitivity analysis. The results show that the hydraulic conductivity of R0 dominates Q_{eq} in the repository area. Specifically, Q_{eq} will not fulfill the safety function indicator for the acceptable hydrogeological condition in the geosphere when the hydraulic conductivity of R# is 1.0 $\times$ 10^{-9} m/s. Although all F values are higher than the safety function indicator for the acceptable hydrogeological condition in the geosphere (i.e., higher than 1.0 $\times$ 10^4 year/m), there are few values smaller than the 1.0 $\times$ 10^6 year/m, which is relatively low in this study.

Table 4. The maximum and minimum values of Q_{eq} and F for the base case and the sensitivity analysis cases.

Cases	Base Case	R0_5.0 × 10^{-6}	R0_1.0 × 10^{-4}	R#_1.0 × 10^{-12}	R#_1.0 × 10^{-9}	F#_1.0 × 10^{-8}	F#_1.0 × 10^{-4}	EDZ_3.3 × 10^{-9}	EDZ_3.3 × 10^{-7}
Maximum Q_{eq} (m^3/year)	8.72×10^{-5}	9.01×10^{-5}	6.08×10^{-5}	4.12×10^{-5}	1.91×10^{-4}	7.39×10^{-5}	6.07×10^{-5}	7.67×10^{-5}	7.53×10^{-5}
Minimum Q_{eq} (m^3/year)	4.55×10^{-5}	4.69×10^{-5}	1.32×10^{-5}	5.88×10^{-6}	1.49×10^{-4}	4.55×10^{-5}	3.76×10^{-5}	4.62×10^{-5}	4.48×10^{-5}
Maximum F (year/m)	4.78×10^{7}	6.15×10^{7}	7.61×10^{8}	5.91×10^{8}	2.33×10^{7}	6.17×10^{7}	6.83×10^{7}	5.33×10^{7}	5.29×10^{7}
Minimum F (year/m)	2.51×10^{6}	2.54×10^{6}	5.78×10^{6}	1.51×10^{7}	7.77×10^{5}	1.41×10^{6}	4.29×10^{6}	2.24×10^{6}	1.88×10^{6}

4.3. The Stochastic Simulations for 49 DFN Realizations

4.3.1. Effective Fracture Number

Table 5 shows the calculations of the effective fracture numbers for the 49 DFN realizations. Here, we have focused on the univariate description of the parameters, i.e., M, SD, Max, and Min. Note that the realization numbers in Table 5 are to give the specific names for different realizations. Table 6 lists these parameters and their relative realization numbers. We then focus on modeling the flow field and particle tracking and calculate the PMs for the realizations. Figure 13a shows Q_{eq} for the Q1 path of the realizations relative to the statistical results of effective fracture numbers. The result shows that the realization number 51 has the highest Q_{eq} 8.11×10^{-5} m^3/year, which meets the scenario with the highest effective fracture number. The realization number 06 has the lowest Q_{eq} 1.77×10^{-5} m^3/year, but this realization represents the statistical result for M + 1 SD, which doesn't meet the scenario for the minimum Q_{eq}. The trends for all the results are very similar, except for the realization number 06, which has lower values when the fraction is lower than 30%. We found that some small fractures intersect the DH and remain in the simulation domain. These small fractures could lead to extremely small Q_{eq} values. However, all Q_{eq} values fulfill the safety function indicator, i.e., lower than 1.0×10^{-4} m^3/year.

Table 5. The effective fracture numbers of the 49 DFN realizations.

Realization number *	01	02	03	04	05	06	07	08	09
Fracture number **	8,320,632	8,341,248	8,156,556	8,278,347	8,285,150	8,300,106	8,239,884	8,225,342	8,252,640
Realization number	11	21	31	41	51	61	71	81	91
Fracture number *	8,195,941	8,253,067	8,237,262	8,265,553	8,385,158	8,264,897	8,301,048	8,241,552	8,230,608
Realization number	12	22	32	42	52	62	72	82	92
Fracture number *	8,273,013	8,231,334	8,253,960	8,279,343	8,308,163	8,206,153	8,269,453	8,219,716	8,210,454
Realization number	13	23	33	43	53	63	73	83	93
Fracture number *	8,235,503	8,353,253	8,258,874	8,214,399	8,304,313	8,186,264	8,205,598	8,238,796	8,295,528
Realization number	14	24	34	44	54	64	74	84	94
Fracture number *	8,246,436	8,204,342	8,267,200	8,245,352	8,247,883	8,243,216	8,273,206	8,241,587	8,228,915
Realization number	10	20	30	40	-	-	-	-	-
Fracture number *	8,182,334	8,269,977	8,191,695	8,283,339	-	-	-	-	-

* The realization number is only for defining the name of the realization. ** The values have been rounded to the nearest whole number.

Figure 13b shows F for the Q1 path of the realizations relative to the statistical results of the effective fracture number. The result shows that the realization number 03 has the highest value, which is 6.66×10^{7} year/m, and it meets the scenario with the lowest effective fracture number. The realization 06 has the minimum F value of 1.95×10^{6} m^3/year, but this realization represents the statistical result for M + 1 SD, which doesn't meet the scenario for the lowest F. The trends for all the results are similar, except for the realization number 06, which has lower values when the fraction is lower than 5%. The reason could be that the very small fractures intersect the DHs and remain in the simulation domain since they are connected fractures. These very small fractures improve the fracture connection and increase the transport velocity. However, all values obtained from the DFN realizations fulfill the safety function indicator for F, i.e., higher than 1.0×10^4 year/m. In summary, the statistics for the effective fracture number of 49 realizations indicate a low impact of DFN realizations on the results of Q_{eq} and F.

Table 6. Statistical summary of the effective fracture numbers for the 49 DFN realizations.

Parameters	Effective Fracture Number *	Realization Number
Min	8,156,556	03
Max	8,385,158	51
M	8,253,971	32
SD	45,126	-
M − 3 SD	8,118,592	- **
M − 2 SD	8,163,718	03
M − 1 SD	8,208,845	92
M + 1 SD	8,299,098	06
M + 2 SD	8,344,224	02
M + 3 SD	8,389,351	51

* The values have been rounded to the nearest whole number. ** There is no realization that meets the effective fracture number for M − 3 SD.

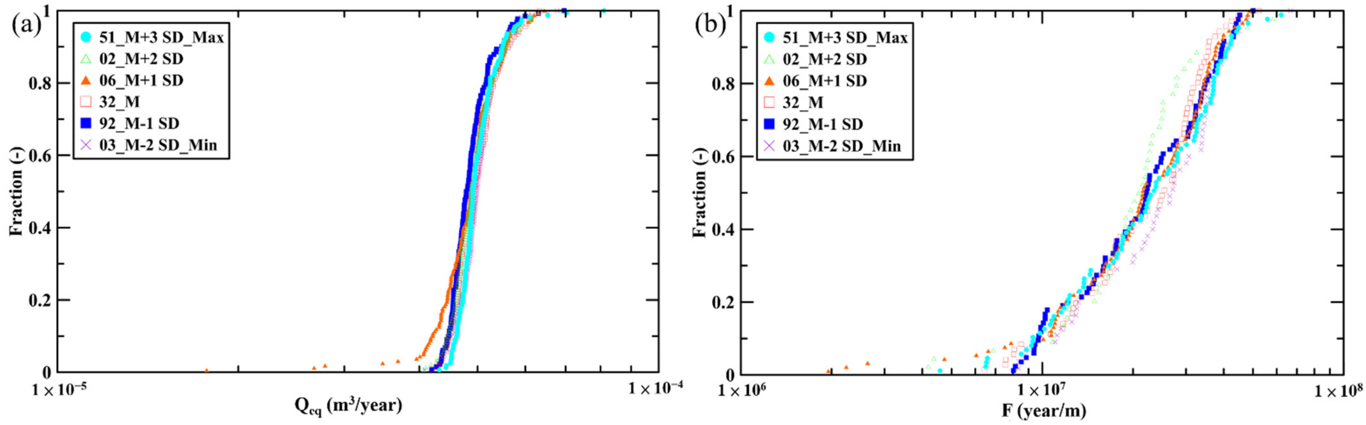

Figure 13. Q_{eq} and F of the realizations relative to the statistical results of the effective fracture numbers. (**a**) The results of Q_{eq} for the statistics of the effective fracture numbers; (**b**) The results of F for the statistics of the effective fracture numbers.

4.3.2. Remaining DHs Based on Rejection Criteria for the Q1 Path

Table 7 shows the remaining DHs after involving the rejection criteria for the Q1 path of the 49 DFN realizations. Table 8 lists the statistics and their relative realization numbers. We then focus on modeling the flow field and particle tracking and calculate the PMs for these selected realizations. Figure 14a shows Q_{eq} for the Q1 path based on the realizations and the associated remaining numbers of the DHs. The result shows that the realization number 41 has the highest Q_{eq} with 7.76×10^{-5} m^3/year), which meets the scenario with the highest remaining number of DHs. The realization number 72 has the lowest Q_{eq} with 3.84×10^{-5} m^3/year, but this realization represents the statistical result for M + 2 SD, which doesn't meet the scenario for the lowest Q_{eq}. The overall trends for all the results are similar. However, all the values fulfill the safety function indicator for Q_{eq} for the acceptable hydrogeological condition in the geosphere, i.e., lower than 1.0×10^{-4} m^3/year.

Table 7. The remaining numbers of DHs based on the rejection criteria applied to the 49 DFN realizations.

Realization number *	01	02	03	04	05	06	07	08	09
Number of DH **	138	128	139	153	150	147	167	113	133
Realization number	11	21	31	41	51	61	71	81	91
Number of DH	132	141	152	168	142	142	143	153	114
Realization number	12	22	32	42	52	62	72	82	92
Number of DH	125	125	126	121	132	128	165	132	122
Realization number	13	23	33	43	53	63	73	83	93
Number of DH	138	112	133	130	140	146	130	148	139
Realization number	14	24	34	44	54	64	74	84	94
Number of DH	128	115	129	124	132	117	152	146	144
Realization number	10	20	30	40	-	-	-	-	-
Number of DH	148	142	149	126	-	-	-	-	-

* The realization number is only for defining the names of different realizations. ** The values have been rounded to the nearest whole number.

Table 8. Statistics of the remaining number of DHs after involving the rejection criteria for the Q1 paths obtained from the 49 realizations.

Parameters	Remaining Number of DH *	Realization
Min.	112	23
Max.	168	41
M	137	1, 13
SD	14	-
M − 3 SD	96	- **
M − 2 SD	109	23
M − 1 SD	123	92
M + 1 SD	150	5
M + 2 SD	164	72
M + 3 SD	178	- **

* The values have been rounded to the nearest whole number. ** No realization meets the remaining number of DH for M − 3 S.D and M + 3 SD.

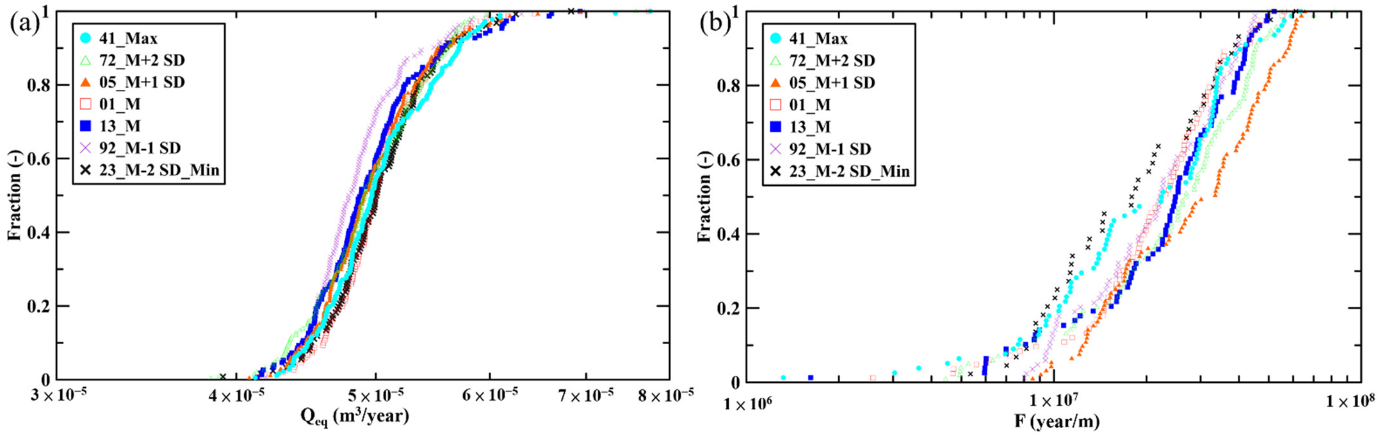

Figure 14. Q_{eq} and F of the realizations relative to the statistical results of the remaining number of DHs after involving the rejection criteria for the Q1 path. (**a**) The results of Q_{eq} for the statistical results of the remaining number of DHs after involving the rejection criteria; (**b**) The results of F for the statistical results of the remaining number of DHs after involving the rejection criteria.

Figure 14b shows F for the Q1 path of the DFN realizations. The result indicates that realization number 72 shows the highest value of 8.19×10^7 year/m, but this realization represents the statistical result for M + 2 SD. On the other hand, realization 41 yields the lowest F value of 1.32×10^6 year/m, but this realization represents the statistical result for Max. The trends for all the results are similar, except for realization 41, which has lower values when the fraction is lower than 5%. The results might be induced by the small fractures connected to the DHs. However, all F values fulfill the safety function indicator for the acceptable hydrogeological condition in the geosphere, i.e., higher than 1.0×10^4 year/m. In summary, the simulations for the remaining DHs obtained from the 49 realizations show a negligible impact on the results of Q_{eq} and F. The uncertainty induced by the DFN realization is relatively small.

5. Conclusions

This study developed and presented the flow and advective transport simulation in fractured rock. Specifically, we involved a reference case composed of a conceptual repository and a fractured rock in the simulation domain. The study employed DarcyTools for modeling the flow and advective transport of a radioactive waste geological repository in fractured rocks based on the KBS-3 disposal concept. This study also used three proposed tasks to model the base case and conduct sensitivity and uncertainty analyses. We compared the solutions of PMs in the tasks with the safety function indicator for the acceptable hydrogeological condition in the geosphere. In this study, we focused on the Q1 path that represents the concept of radionuclides leaving the canisters.

The numerical modeling domain considered the geometry and flow properties of components of a conceptual repository (i.e., MT, DT, DH, and EDZ). The study applied the cell refinement algorithm to generate computational grids for the important hydrogeological units and components in the repository. The successive refinement led to a total number of 11,613,681 cells. In the example DFN case, the total number of 8,182,334 fractures was generated. Based on the generated fractures, the fracture connectivity analysis enabled the identification of intersections between fractures and the key components in the repository. The effective fracture system was then obtained by removing the isolated fractures and was the basis for the up-scaled flow properties in each computational cell.

After involving the rejection criteria in the base case, the study calculated the remaining DH and obtained 148 DHs for the Q1 paths based on the KBS-3 disposal concept. The PMs calculations showed that the maximum value of Q_{eq} was 8.72×10^{-5} m^3/year, which fulfilled the requirements of the safety function (i.e., lower than 1.0×10^{-4} m^3/year). The minimum F value was 2.51×10^6 year/m, which also fulfilled the requirements of the safety function (i.e., higher than 1.0×10^4 year/m).

In the study, there are eight cases selected for the sensitivity analysis. An additional 48 DFN realizations were used for the uncertainty analysis. The sensitivity analysis showed that the case with a host rock hydraulic conductivity of 1.0×10^{-9} m/s yielded the highest Q_{eq} of 1.91×10^{-4} m^3/year and lowest F of 7.77×10^5 year/m. In this case, Q_{eq} did not fulfill the safety function indicator for the acceptable hydrogeological condition in the geosphere. Although all F values were higher than the safety function indicator, few values were smaller than 1.0×10^6 year/m, which was relatively low in this study. The statistical results for the 49 realizations relative to the effective fracture number showed that the realization number 51 had the highest Q_{eq} of 8.11×10^{-5} m^3/year, and the realization number 06 had the lowest F of 1.95×10^6 year/m. The statistical results for the 49 realizations relative to the remaining number of DHs after involving the rejection criteria showed that the realization number 41 had the highest Q_{eq} of 7.76×10^{-5} m^3/year and the realization number 41 had the lowest F of 1.32×10^6 year/m. Simulation results revealed that the overall behavior of DHs in the 49 realizations is similar, indicating less impact of fracture distribution on F and Q_{eq} for the proposed reference case in the study. In addition, all values fulfill the safety function indicator for the acceptable hydrogeological condition in the geosphere. The solutions were critical for evaluating the radionuclides released from the repository for performance and safety assessment in the radioactive waste geological disposal. Results indicated that the hydraulic conductivity variations of the hydrogeological units are critical for F and Q_{eq}. The DFN realizations with different fracture distributions might not be significant for the variations of F and Q_{eq}.

Author Contributions: Conceptualization, Y.-C.Y. and Y.-H.S.; methodology, Y.-C.Y. and Y.-H.S.; software, Y.-C.Y., Y.-H.S. and T.-P.L.; validation, Y.-C.Y. and Y.-H.S.; resources, T.-P.L.; data curation, Y.-C.Y. and Y.-H.S.; writing—original draft preparation, Y.-C.Y. and Y.-H.S.; writing—review and editing, T.-P.L., C.-F.N. and I.-H.L.; visualization, Y.-C.Y., Y.-H.S. and I.-H.L.; supervision, T.-P.L.; project administration, T.-P.L.; funding acquisition, T.-P.L. All authors have read and agreed to the published version of the manuscript.

Funding: This research was funded by Taiwan Power Company, Taiwan (ROC), grant number 078090902101.

Institutional Review Board Statement: No application.

Informed Consent Statement: No application.

Data Availability Statement: All data are presented in this article in the form of figures and tables.

Conflicts of Interest: The authors declare no conflict of interest.

References

1. Hyman, J.D.; Gable, C.W.; Painter, S.L.; Makedonska, N. Conforming delaunay triangulation of stochastically generated three dimensional discrete fracture networks: A feature rejection algorithm for meshing strategy. *J. Sci. Comput.* **2014**, *36*, A1871–A1894. [CrossRef]
2. Hyman, J.D.; Karra, S.; Makedonska, N.; Gable, C.W.; Painter, S.L.; Viswanathan, H.S. dfnWorks: A discrete fracture network framework for modeling subsurface flow and transport. *Comput. Geosci.* **2015**, *84*, 10–19. [CrossRef]
3. Kalbacher, T.; Wang, W.; McDermott, C.; Kolditz, O.; Taniguchi, T. Development and application of a CAD interface for fractured rock. *Eng. Geol.* **2005**, *47*, 1017–1027. [CrossRef]
4. Makedonska, N.; Painter, S.; Bui, Q.; Gable, C.; Karra, S. Particle tracking approach for transport in three-dimensional discrete fracture networks. *Comput. Geosci.* **2015**, *19*, 1123–1137. [CrossRef]
5. Zhang, Q.H. Finite element generation of arbitrary 3-D fracture networks for flow analysis in complicated discrete fracture networks. *J. Hydrol.* **2015**, *529*, 890–908. [CrossRef]
6. Chen, R.H.; Lee, C.H.; Chen, C.S. Evaluation of transport of radioactive contaminant in fractured rock. *Environ. Geol.* **2001**, *41*, 440–450. [CrossRef]
7. Jing, L. A review of techniques, advances and outstanding issues in numerical modelling for rock mechanics and rock engineering. *Int. J. Min. Reclam. Environ.* **2003**, *40*, 283–353. [CrossRef]
8. Rutqvist, J.; Leung, C.; Hoch, A.; Wang, Y.; Wang, Z. Linked multicontinuum and crack tensor approach for modeling of coupled geomechanics, fluid flow and transport in fractured rock. *J. Rock Mech. Geotech. Eng.* **2013**, *5*, 18–31. [CrossRef]
9. Svensson, U.; Follin, S. *Groundwater Flow Modelling of Excavation and Operational Phase—Forsmark*; R-09-19; Svensk Kärnbränslehantering AB: Stockholm, Sweden, 2010.
10. Vidstrand, P.; Follin, S.; Zugec, N. *Groundwater Flow Modelling of Periods with Periglacial and Glacial Climate Conditions—Forsmark*; R-09-21; Svensk Kärnbränslehantering AB: Stockholm, Sweden, 2010.
11. Selroos, J.-O.; Follin, S. *SR-Site Groundwater flow Modelling Methodology, Setup and Results*; R-09-22; Svensk Kärnbränslehantering AB: Stockholm, Sweden, 2010.
12. Nuclear Materials and Radioactive Waste Management Act. Available online: https://erss.aec.gov.tw/law/EngLawContent.aspx?lan=E&id=6 (accessed on 30 June 2022).
13. Enforcement Rules for the Nuclear Materials and Radioactive Waste Management Act. Available online: https://law.moj.gov.tw/ENG/LawClass/LawAll.aspx?pcode=J0160034 (accessed on 19 July 2022).
14. Taiwan Power Company. *The Preliminary Technical Feasibility Study for Final Disposal of Spent Nuclear Fuel–2009 Progress Report (Summary)*; Taiwan Power Company: Taipei, Taiwan, 2009.
15. Swedish Nuclear Fuel Supply Company. *Final Storage of Spent Nuclear Fuel–KBS-3 (Summary)*; Swedish Nuclear Fuel Supply Company/Division KBS: Stockholm, Sweden, 1983.
16. Taiwan Power Company. *The Technical Feasibility Assessment Report on Spent Nuclear Fuel Final Disposal, Main Report*; Potential Host Rock Characterization and Evaluation Stage; The Spent Nuclear Fuel Final Disposal Program; Taiwan Power Company: Taipei, Taiwan, 2017.
17. Japan Nuclear Cycle Development Institute. *H12: Project to Establish the Scientific and Technical Basis for HLW Disposal in Japan, Project Overview Report*; Second Progress Report on Research and Development for the Geological Disposal of HLW in Japan; Japan Nuclear Cycle Development Institute: Tokyo, Japan, 2000.

18. Svensk Kärnbränslehantering AB. *Site Description of Forsmark at Completion of the Site Investigation Phase, SDM-Site Forsmark*; TR-08-05; Svensk Kärnbränslehantering AB: Stockholm, Sweden, 2008.
19. Joyce, S.; Simpson, T.; Hartley, L.; Applegate, D.; Hoek, J.; Jackson, P.; Swan, D. *Groundwater Flow Modelling of Periods with Temperate Climate Conditions—Forsmark*; R-09-20; Svensk Kärnbränslehantering AB: Stockholm, Sweden, 2010.
20. Svensk Kärnbränslehantering AB. *Long-Term Safety for the Final Repository for Spent Nuclear Fuel at Forsmark, Main Report of the DR-Site Project*; TR-11-01; Svensk Kärnbränslehantering AB: Stockholm, Sweden, 2011.
21. Svensk Kärnbränslehantering AB; POSIVA Oy. *Safety Functions, Performance Targets and Technical Design Requirements for a KBS-3V Repository, Conclusion and Recommendations from a Joint SKB and Posiva Working Group*; Posiva SKB Report, 01; Svensk Kärnbränslehantering AB: Stockholm, Sweden; POSIVA Oy: Eurajoki, Finland, 2017.
22. Svensson, U. A continuum representation of fracture networks. Part I: Method and basic test cases. *J. Hydrol.* **2001**, *250*, 170–186. [CrossRef]
23. Svensson, U. A continuum representation of fracture networks. Part II: Application to the Äspö Hard Rock laboratory. *J. Hydrol.* **2001**, *250*, 187–205. [CrossRef]
24. Svensson, U.; Ferry, M. DarcyTools: A computer code for hydrogeological analysis of nuclear waste repositories in fractured rock. *J. Appl. Math. Phys.* **2014**, *2*, 365–383. [CrossRef]
25. Svensson, U.; Kuylenstierna, H.-O.; Ferry, M. *DarcyTools Version 3.4–Concepts, Methods and Equations*; R-07-38; Svensk Kärnbränslehantering AB: Stockholm, Sweden, 2010.
26. Svensson, U. *DarcyTools Version 3.4–Verification, Validation and Demonstration*; R-10-71; Svensk Kärnbränslehantering AB: Stockholm, Sweden, 2010.
27. Svensson, U.; Ferry, M. *DarcyTools Version 3.4–User's Guide*; R-10-72; Svensk Kärnbränslehantering AB: Stockholm, Sweden, 2010.
28. Moreno, L.; Gylling, B. *Equivalent Flow Rate Concept Used in Near Field Transport Model COMP23–Proposed Value for SR-97*; R-98-53; Svensk Kärnbränslehantering AB: Stockholm, Sweden, 1998.
29. Andersson, J.; Elert, M.; Gylling, B.; Moreno, L.; Selroos, J.-O. *Derivation and Treatment of the Flow Wetted Surface and Other Geosphere Parameters in the Transport Models FARF31 and COMP23 for Use in Safety Assessment*; R-98-60; Svensk Kärnbränslehantering AB: Stockholm, Sweden, 1998.
30. Lee, T.P. Construction of DFN-Based Hydrogeological Model Using Reference Case Data for SNF Disposal in Taiwan. ARMA-DFNE-18-0820. In Proceedings of the 2nd International Discrete Fracture Network Engineering Conference, Seattle, WA, USA, 20 June 2018.
31. Chiu, T.-H. The Application of Discrete Fracture Network Model for Taiwan SNF Final Disposal Program. ARMA-DFNE-18-0919. In Proceedings of the 2nd International Discrete Fracture Network Engineering Conference, Seattle, WA, USA, 20 June 2018.
32. Liou, T.-S.; Huang, S.-Y.; Tien, N.-C.; Lin, W.; Lin, C.-K. Characterization of Groundwater Flow in a Fractured Crystalline Rock Mass Using Taiwan's Reference Case Data. ARMA-DFNE-18-0285. In Proceedings of the 2nd International Discrete Fracture Network Engineering Conference, Seattle, WA, USA, 20 June 2018.
33. Svensk Kärnbränslehantering AB. *Buffer, Backfill and Closure Process Report for the Safety Assessment SR-Site*; TR-10-47; Svensk Kärnbränslehantering AB: Stockholm, Sweden, 2010.
34. Bäckblom, G. *Excavation Damage and Disturbance in Crystalline Rock–Results from Experiments and Analyses*; TR-08-08; Svensk Kärnbränslehantering AB: Stockholm, Sweden, 2008.